BIOCHEMISTRY

PIK3CA gain-of-function mutation in adipose tissue induces metabolic reprogramming with Warburg-like effect and severe endocrine disruption

Sophia Ladraa[1,2], Lola Zerbib[1,2], Charles Bayard[1,2], Antoine Fraissenon[2,3,4,5], Quitterie Venot[1,2], Gabriel Morin[1,2], Alexandre P. Garneau[1,2], Pierre Isnard[1,6], Célia Chapelle[1,2], Clément Hoguin[2,7], Sylvie Fraitag[6], Jean-Paul Duong[1,6], Laurent Guibaud[2,3], Alix Besançon[1,8], Sophie Kaltenbach[1,9], Patrick Villarese[9], Vahid Asnafi[1,2,9], Christine Broissand[10], Nicolas Goudin[11], Michael Dussiot[1,12], Ivan Nemazanyy[13], Thomas Viel[14], Gwennhael Autret[14], Céline Cruciani-Guglielmacci[1,15], Jessica Denom[1,15], Julie Bruneau[1,6], Bertrand Tavitian[1,14], Christophe Legendre[1,2,16], Julien Dairou[1,17], Jean-Marc Lacorte[18,19], Pacifique Levy[18], Mario Pende[1,2], Michel Polak[1,8], Guillaume Canaud[1,2,7]*

***PIK3CA*-related overgrowth syndrome (PROS) is a genetic disorder caused by somatic mosaic gain-of-function mutations of *PIK3CA*. Clinical presentation of patients is diverse and associated with endocrine disruption. Adipose tissue is frequently involved, but its role in disease development and progression has not been elucidated. Here, we created a mouse model of *PIK3CA*-related adipose tissue overgrowth that recapitulates patient phenotype. We demonstrate that *PIK3CA* mutation leads to GLUT4 membrane accumulation with a negative feedback loop on insulin secretion, a burst of liver IGFBP1 synthesis with IGF-1 sequestration, and low circulating levels. Mouse phenotype was mainly driven through AKT2. We also observed that *PIK3CA* mutation induces metabolic reprogramming with Warburg-like effect and protein and lipid synthesis, hallmarks of cancer cells, in vitro, in vivo, and in patients. We lastly show that alpelisib is efficient at preventing and improving *PIK3CA*-adipose tissue overgrowth and reversing metabolomic anomalies in both animal models and patients.**

INTRODUCTION

PIK3CA-related overgrowth syndrome (PROS) is a rare genetic disorder caused by gain-of-function mutations in the *PIK3CA* gene (*1*). These mutations occur most frequently during embryogenesis and lead to somatic mosaicism (*2*). Phosphatidylinositol-4,5-bisphosphate 3-kinase, catalytic subunit alpha (PIK3CA) is a ubiquitously expressed lipid kinase that controls signaling pathways participating in cell proliferation, motility, survival, and metabolism (*3*).

At the cellular level, PIK3CA is mainly recruited through tyrosine kinase receptors. *PIK3CA* encodes the 110-kDa catalytic alpha subunit of phosphatidylinositol 3-kinase (PI3K; p110α), which converts, at the plasma membrane, phosphatidylinositol 4,5-bisphosphate to phosphatidylinositol 3,4,5-trisphosphate and subsequently recruits phosphoinositide-dependent kinase-1 (PDK1), which, in turn, phosphorylates AKT on the Thr^{308} residue to initiate downstream cellular effects. PIK3CA also regulates many other pathways, including the Rho/Rac1 signaling cascade (*4*).

The clinical presentation of patients with PROS is extremely broad owing to mosaicism and the characteristics of the tissue involved (*5*–*7*). Patients usually have complex tissue malformations, including abnormal vessels, muscle hypertrophy, and/or bone deformation (*1*, *8*–*11*). Adipose tissue is frequently involved (*12*). In addition to adipose tissue overgrowth (also known as fibroadipose hyperplasia, fibroadipose vascular anomaly, facial infiltrating lipomatosis, or lipomatosis of nerve), these patients usually present with unexplained hormonal dysregulation and metabolic anomalies such as low circulating insulin-like growth factor 1 (IGF-1) level and chronic hypoglycemia (*13*–*16*).

We recently generated a mouse model of PROS using ubiquitously expressed inducible *Cre* recombinase (*CAGG* Cre^{ER}) (*17*). However, this mouse model did not allow us to determine the role specifically played by adipose tissue in PROS physiopathology. We therefore decided to explore the consequence of *PIK3CA* gain-of-function mutations, specifically in adipocytes.

[1]Université Paris Cité, Paris, France. [2]INSERM U1151, Institut Necker-Enfants Malades, Paris, France. [3]Service d'Imagerie Pédiatrique, Hôpital Femme-Mère-Enfant, HCL, Bron, France. [4]CREATIS UMR 5220, Villeurbanne 69100, France. [5]Service de Radiologie Mère-Enfant, Hôpital Nord, Saint Etienne, France. [6]Service d'Anatomie pathologique, Hôpital Necker-Enfants Malades, AP-HP, Paris, France. [7]Unité de médecine translationnelle et thérapies ciblées, Hôpital Necker-Enfants Malades, AP-HP, Paris, France. [8]Service d'Endocrinologie, Gynécologie et Diabétologie Pédiatrique, Centre des maladies endocriniennes rares de la croissance et du développement, Hôpital Necker-Enfants Malades, AP-HP, Paris, France. [9]Laboratoire d'Oncohématologie, Hôpital Necker-Enfants Malades, AP-HP, Paris, France. [10]Pharmacie, Hôpital Necker-Enfants Malades, AP-HP, Paris, France. [11]Necker Bio-Image Analysis, INSERM US24/CNRS UMS 3633, Paris, France. [12]INSERM U1163, Laboratory of Cellular and Molecular Mechanisms of Hematological Disorders and Therapeutic Implications, Laboratoire d'Excellence GR-Ex, Paris, France. [13]Platform for Metabolic Analyses, Structure Fédérative de Recherche Necker, INSERM US24/CNRS UMS 3633, Paris, France. [14]Plateforme Imageries du Vivant, Université de Paris, PARCC, INSERM, Paris, France. [15]Unité de Biologie Fonctionnelle et Adaptative, CNRS, Paris, France. [16]Service de Néphrologie, Transplantation Adultes, Hôpital Necker-Enfants Malades, AP-HP, Paris, France. [17]Laboratoire de Chimie et de Biochimie Pharmacologiques et Toxicologiques, CNRS, Paris, France. [18]Laboratoire de Biochimie Endocrinienne et Oncologique, Hôpital La Pitié Salpêtrière, AP-HP, Paris, France. [19]Sorbonne Université, Paris, France.
*Corresponding author. Email: guillaume.canaud@inserm.fr

RESULTS

Mouse model of adipose tissue overgrowth

We started by breeding the *R26StopFLP110** mouse strain with *Adiponectin Cre* mice to generate *PIK3CA*$^{Adipo\text{-}CreER}$ animals that express a constitutively overactivated form of PIK3CA upon tamoxifen administration. To follow *Cre* recombination, *PIK3CA*$^{Adipo\text{-}CreER}$ mice were then interbred with *Gt(ROSA)26Sor*$^{tm4(ACTB\text{-}tdTomato\text{-}EGFP)Luo/J}$ mice (*18*). In all tissues, these mice express a cell membrane–localized tdTomato fluorescent protein that is replaced by green fluorescent protein (GFP) after *Cre* recombination.

To overcome developmental issues, we used 6-week-old mice that were treated with a daily dose of tamoxifen (40 mg kg^{-1}) for 5 days to induce *Cre* recombination. We observed that starting 2 weeks after *Cre* recombination, *PIK3CA*$^{Adipo\text{-}CreER}$ mice progressively gained weight compared to their wild-type littermates (*PIK3CA*^{WT}) for up to 24 weeks (i.e., the latest follow-up; Fig. 1A and fig. S1A). This was the case for both males and females. We first decided to study mice 6 weeks after tamoxifen administration (i.e., at 12 weeks of age) when the phenotype was well established. Whole-body magnetic resonance imaging (MRI) revealed a subcutaneous and perivisceral adipose tissue content in *PIK3CA*$^{Adipo\text{-}CreER}$ mice approximately double than that in controls (Fig. 1B) associated with significant skeletal muscle reduction (fig. S1B). We euthanized 20 controls and 20 *PIK3CA*$^{Adipo\text{-}CreER}$ mice 6 weeks after tamoxifen administration. Necropsy examination showed not only severe and diffuse adipose tissue infiltration but also a reduction in the size of different organs in *PIK3CA*$^{Adipo\text{-}CreER}$ mice compared to control littermates (fig. S1, C and D). We confirmed that mutant p110α (p110*) and GFP were expressed only in the adipose tissue of *PIK3CA*$^{Adipo\text{-}CreER}$ mice (Fig. 1C and fig. S1, E to G). Using flow cytometry experiments, we observed that the GFP was expressed at a low percentage in adipocyte precursors of both control and mutant mice but did not expand in the *PIK3CA*$^{Adipo\text{-}CreER}$ mice following *Cre* recombination (fig. S1H). As expected, Western blot and immunofluorescence studies showed AKT/mechanistic target of rapamycin (mTOR) pathway activation in white adipose tissue (WAT) (Fig. 1, D to F) and brown adipose tissue (BAT; fig. S2, A and B) of *PIK3CA*$^{Adipo\text{-}CreER}$ mice. Histological examination revealed anomalies in WAT and BAT with hypertrophic adipocytes (Fig. 1G and fig. 2C). BAT anomalies were associated with cold sensitivity because *PIK3CA*$^{Adipo\text{-}CreER}$ mice were spontaneously hypothermic (Fig. 1H).

We did not observe any other histological anomalies with the exception of the presence of adipose tissue dissociating striated muscles (Fig. 1I) associated with muscle fiber size reduction (fig. S2D). Mechanistically, PIK3CA is involved in cell growth. Using the Amnis ImageStream System and morphometric quantification, we confirmed that adipocytes isolated from WAT of *PIK3CA*$^{Adipo\text{-}CreER}$ mice were hypertrophic compared to controls (Fig. 1, J and K). Immunostaining and flow cytometry analysis showed increased adipose tissue infiltration by F4/80^{+} CD11b^{+} cells in *PIK3CA*$^{Adipo\text{-}CreER}$ mice compared to controls (Fig. 1L and fig. S2E). Blood sampling examination revealed nonregenerative anemia with a low white blood cell count in *PIK3CA*$^{Adipo\text{-}CreER}$ mice. Both lymphocyte and neutrophil counts were reduced (Fig. 1M). Blood and bone marrow flow cytometry analysis revealed peripheral T-CD8^{+} and B cell reductions (fig. S2, F and G). Bone marrow analysis showed a moderate decrease in cellularity, with an increased dilated capillary network and no maturation disorders (fig. S2H). We thus created a mouse model that recapitulates the adipose tissue overgrowth that we observed in a subset of patients with PROS.

Hormonal dysregulation

Adipose tissue is a metabolically dynamic organ that synthetizes a certain number of hormones and participates in metabolic homeostasis. PROS patients with adipose tissue involvement often present with metabolic and hormonal dysregulation, such as hypoglycemia and low circulating levels of IGF-1 (*13*). Hence, we decided to explore the consequences of *PIK3CA* gain-of-function mutations in adipose tissue on hormones and metabolism. We first examined the expression of adiponectin and leptin, two hormones extremely sensitive to adipose tissue content. We observed in *PIK3CA*$^{Adipo\text{-}CreER}$ mice low adiponectin expression in adipose tissue (Fig. 2A and fig. S3, A and B) with increased levels of circulating leptin (Fig. 2B). *PIK3CA*$^{Adipo\text{-}CreER}$ mice demonstrated increased food intake with slightly reduced nocturnal energy expenditure (fig. S3C). To better understand the increase in food intake and the high leptin levels, we explored whether *PIK3CA*$^{Adipo\text{-}CreER}$ mice were leptin resistant. We observed that, whereas acute intraperitoneal leptin injection induced hypothalamic signal transducer and activator of transcription 3 (STAT3) phosphorylation in control mice, leptin injection was not associated with hypothalamic STAT3 phosphorylation in *PIK3CA*$^{Adipo\text{-}CreER}$ mice evocative of leptin resistance (fig. S3D).

PIK3CA$^{Adipo\text{-}CreER}$ mice exhibited lower serum creatinine, cholesterol, triglyceride, and nonesterified fatty acid (NEFA) levels than controls (Fig. 2, C and D, and fig. S3E). Reduced NEFA level in *PIK3CA*$^{Adipo\text{-}CreER}$ mice was consistent with inhibition of lipolysis through PIK3CA activation in adipocytes (*19*). Subsequently, the expression of several proteins involved in lipogenesis was increased in WAT of *PIK3CA*$^{Adipo\text{-}CreER}$ mice (fig. S4, A and B). Because NEFAs are major precursors of ketone bodies, we explored whether fasted condition was associated with abnormal ketosis. Control and *PIK3CA*$^{Adipo\text{-}CreER}$ mice were starved, and circulating β-hydroxybutyrate levels were measured. After 12 hours of starvation, we did not observe any difference between controls and *PIK3CA*$^{Adipo\text{-}CreER}$ mice, indicating that ketosis remained unaffected (fig. S5A).

Excess adipose tissue is usually associated with insulin resistance; thus, we next investigated glycemic control in our *PIK3CA*$^{Adipo\text{-}CreER}$ mouse model. We observed that compared to controls, *PIK3CA*$^{Adipo\text{-}CreER}$ mice were hypoglycemic after fasting (Fig. 2E). Hypoglycemia was even more severe in the homozygous mutant of *PIK3CA* (referred to as *PIK3CA*^{HO}), which died rapidly after *Cre* recombination from severe spontaneous hypoglycemia even without fasting (fig. S5B). Pancreas histological examination of the *PIK3CA*$^{Adipo\text{-}CreER}$ mice revealed no difference in β islet size compared to controls (Fig. 2F and fig. S5C). However, circulating insulin levels were reduced (Fig. 2G), with consistent decreased expression of insulin receptors in WAT (fig. S5, D and E). Consistently, pancreatic insulin immunofluorescent staining showed reduced expression in *PIK3CA*$^{Adipo\text{-}CreER}$ mice compared to controls (fig. S5F). The intraperitoneal glucose tolerance test showed a normal insulin response (Fig. 2H).

We next explored endogenous glucose production in controls and *PIK3CA*^{AdipoCreER} mice. We used two different approaches. First, we administrated pyruvate intraperitoneally and observed

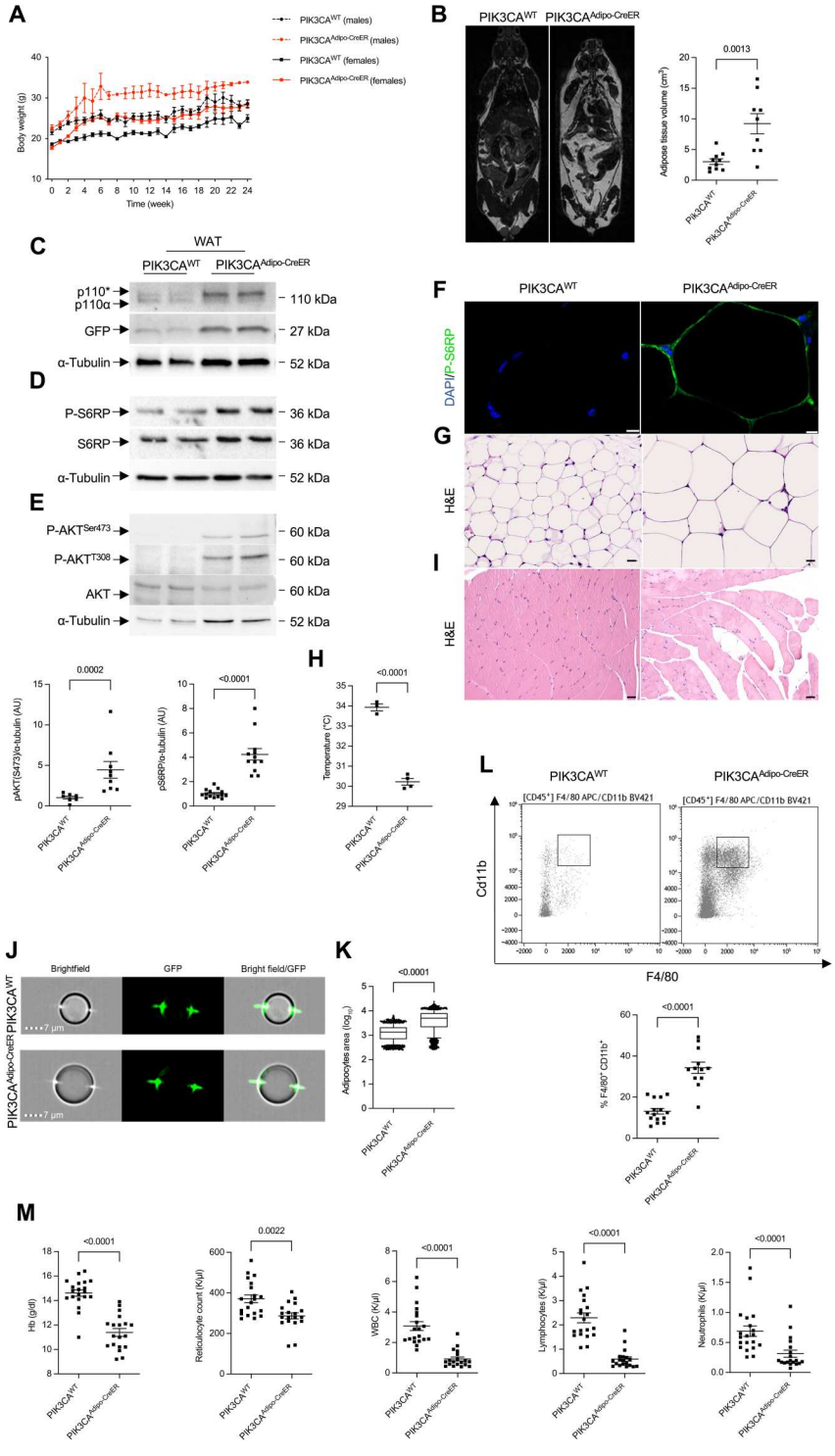

Fig. 1. A mouse model of *PIK3CA*-related adipose tissue overgrowth. (**A**) Male and female body weights of *PIK3CA*^{WT} and *PIK3CA*$^{Adipo\text{-}CreER}$ (n = 20 per group) mice after *Cre* recombination. (**B**) Coronal whole-body T2-weighted magnetic resonance images (MRIs) of *PIK3CA*^{WT} and *PIK3CA*$^{Adipo\text{-}CreER}$ mice (n = 9 mice per group). Adipose tissue volume quantification. (**C**) Western blot of p110 and GFP in WAT of *PIK3CA*^{WT} and *PIK3CA*$^{Adipo\text{-}CreER}$ mice. (**D**) Western blot and quantification of P-S6RP in WAT of *PIK3CA*^{WT} and *PIK3CA*$^{Adipo\text{-}CreER}$ mice (n = 12 per group). AU, arbitrary units. (**E**) Western blot and quantification of AKT phosphorylation on residues Ser^{473} and Th^{308} in WAT of *PIK3CA*^{WT} (n = 7) and *PIK3CA*$^{Adipo\text{-}CreER}$ mice (n = 9). (**F**) Representative immunofluorescence of P-S6RP in WAT of *PIK3CA*^{WT} and *PIK3CA*$^{Adipo\text{-}CreER}$ mice. Scale bar, 10 µm. (**G**) Representative hematoxylin and eosin (H&E) staining of WAT of *PIK3CA*^{WT} and *PIK3CA*$^{Adipo\text{-}CreER}$ mice. Scale bar, 10 µm. (**H**) *PIK3CA*^{WT} and *PIK3CA*$^{Adipo\text{-}CreER}$ mice body temperature (room temperature is 21°C). (**I**) Representative H&E staining of striated muscles of *PIK3CA*^{WT} and *PIK3CA*$^{Adipo\text{-}CreER}$ mice. Scale bar, 10 µm. (**J**) Representative images of WAT adipocytes isolated from *PIK3CA*^{WT} and *PIK3CA*$^{Adipo\text{-}CreER}$ mice using Amnis ImageStream. (**K**) Quantification of adipocyte cell area of *PIK3CA*^{WT} and *PIK3CA*$^{Adipo\text{-}CreER}$ mice (n = 5 mice per group). (**L**) Cd11b and F4/80 flow cytometry experiment and quantification in WAT of *PIK3CA*^{WT} (n = 15) and *PIK3CA*$^{Adipo\text{-}CreER}$ mice (n = 15). (**M**) Blood sampling examination in *PIK3CA*^{WT} and *PIK3CA*$^{Adipo\text{-}CreER}$ mice (n = 20 mice per group).

an increase in blood glucose production in both types of mice (fig. S6A). Second, we measured in the liver of control and *PIK3CA*^{AdipoCreER} mice the levels of enzymes involved in gluconeogenesis. Except for a significant reduction at the mRNA level of pyruvate carboxylase in mutant mice, which was not confirmed at the protein level, we did not observe any difference (fig. S6, B and C). We concluded that endogenous glucose production remained unaffected in *PIK3CA*^{AdipoCreER} mice.

To better characterize the metabolic disruption presented by *PIK3CA*^{AdipoCreER} mice, we explored different parameters in fasted states (12 hours) followed by refed states (3 hours). We observed similar trends in body weight loss between the two groups of mice (fig. S7). However, multiple parameters were transiently

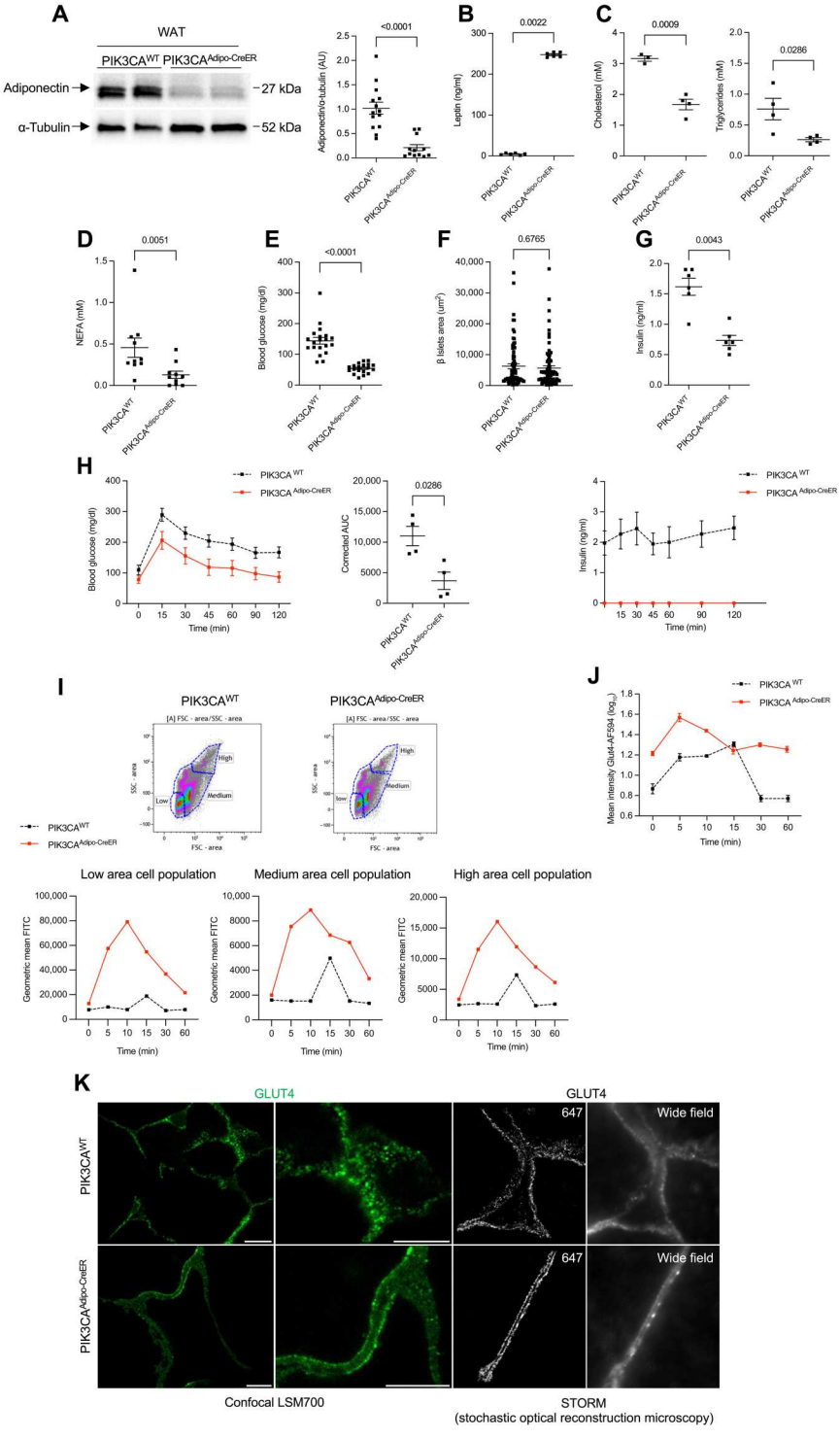

Fig. 2. *PIK3CA*$^{Adipo\text{-}CreER}$ mice present severe hypoglycemia with adipocytes GLUT4 cell membrane recruitment. (**A**) Western blot and quantification of adiponectin in WAT of *PIK3CA*^{WT} ($n = 14$) and *PIK3CA*$^{Adipo\text{-}CreER}$ mice ($n = 12$). (**B**) Leptin circulating levels in *PIK3CA*^{WT} and *PIK3CA*$^{Adipo\text{-}CreER}$ mice ($n = 6$ per group). (**C**) Cholesterol and triglyceride levels in *PIK3CA*^{WT} ($n = 3$) and *PIK3CA*$^{Adipo\text{-}CreER}$ mice ($n = 4$). (**D**) Quantification of circulating levels of NEFA in serum from *PIK3CA*^{WT} and *PIK3CA*$^{Adipo\text{-}CreER}$ mice ($n = 10$ per group). (**E**) Twelve-hour fasted glycemia in *PIK3CA*^{WT} ($n = 18$) and *PIK3CA*$^{Adipo\text{-}CreER}$ mice ($n = 19$). (**F**) β Islet area in *PIK3CA*^{WT} and *PIK3CA*$^{Adipo\text{-}CreER}$ mice ($n = 4$ mice per group). (**G**) Insulin circulating levels in *PIK3CA*^{WT} ($n = 8$) and *PIK3CA*$^{Adipo\text{-}CreER}$ mice ($n = 7$). (**H**) Intraperitoneal glucose tolerance test (GTT) in *PIK3CA*^{WT} and *PIK3CA*$^{Adipo\text{-}CreER}$ mice ($n = 5$ mice per group) and insulin circulating levels at all GTT points. Insulin levels were too low and undetectable in *PIK3CA*$^{Adipo\text{-}CreER}$ mice. (**I**) Glucose uptake in primary culture of adipocytes derived from *PIK3CA*^{WT} and *PIK3CA*$^{Adipo\text{-}CreER}$ mice ($n = 3$ per group). Three different adipocyte population according to their sizes were identified in each group of mice. (**J**) Mean GLUT4 intensity at the cell surface of adipocytes derived from *PIK3CA*^{WT} and *PIK3CA*$^{Adipo\text{-}CreER}$ mice ($n = 5$ mice per group), before and upon insulin stimulation. (**K**) Representative GLUT4 immunofluorescence in WAT of *PIK3CA*^{WT} and *PIK3CA*$^{Adipo\text{-}CreER}$ mice. Scale bar, 10 µm.

corrected such as blood glucose, NEFA, and triglycerides (fig. S7). These findings indicate that, when fed, *PIK3CA*^{AdipoCreER} mice have the ability to partially correct metabolic anomalies.

At the cellular level, glucose uptake from the blood into adipocytes is mainly mediated by the glucose transporter type 4 (GLUT4) transporter after insulin stimulation (*20*). PIK3CA recruits AKT, which, in turn, controls GLUT4 trafficking to the plasma membrane (*21*–*23*). We hypothesized that *PIK3CA* gain-of-function mutation activates AKT and facilitates GLUT4 migration to the cell surface (*24*). We used primary culture of adipocytes from *PIK3CA*^{AdipoCreER} and control mice. We observed that adipocytes derived from *PIK3CA*^{AdipoCreER} demonstrated higher glucose uptake compared to control littermate mice following insulin stimulation (Fig. 2I). We then explored GLUT4 expression in primary culture of

adipocytes derived from controls and *PIK3CA*^{AdipoCreER} mice. Flow cytometry analysis showed GLUT4 accumulation at the cell membrane of adipocytes from *PIK3CA*$^{CAGG\text{-}CreER}$ compared to adipocytes isolated from control mice (Fig. 2J). This accumulation was even increased after insulin stimulation.

Using stochastic optical reconstruction microscopy technology, we then confirmed in vivo that GLUT4 accumulated at the cell membrane of adipocytes in *PIK3CA*$^{Adipo\text{-}CreER}$ mice compared to controls (Fig. 2K). We concluded that *PIK3CA* gain-of-function mutation enhances GLUT4 trafficking to the plasma membrane through AKT activation, which leads to chronic hypoglycemia with negative feedback on the β pancreatic islets and insulin secretion.

Insulin levels correlate with IGF-1, so we decided to measure circulating IGF-1 levels in the *PIK3CA*$^{Adipo\text{-}CreER}$ mouse model. We observed that IGF-1 levels were reduced in *PIK3CA*$^{Adipo\text{-}CreER}$ mice compared to controls (Fig. 3A), which is the most likely explanation for the size reduction observed in organs of *PIK3CA*$^{Adipo\text{-}CreER}$ mice (fig. S1, C and D). However, circulating growth hormone levels were not different between mutant and control mice (Fig. 3B). Liver examination revealed that *IGF-1* mRNA synthesis was similar between *PIK3CA*$^{Adipo\text{-}CreER}$ and control mice (Fig. 3C), but IGF-1 protein was significantly reduced in mutant mice (Fig. 3D). Most IGF-1 molecules are bound by one of the members of the IGF-binding protein (IGFBP) family, of which six distinct types exist. These proteins bind to IGF-1 with an equal or greater affinity than the IGF-1 receptor and are thus in a key position to regulate IGF signaling globally and locally. We therefore measured *IGFBP* mRNA levels in mouse livers. Whereas *IGFBP2* to *IGFBP6* mRNA levels did not or only modestly change (Fig. 3, E to G), we observed an 18-fold increase in the *IGFBP1* mRNA level (Fig. 3H), which was then confirmed at the protein level (Fig. 3I) in *PIK3CA*$^{Adipo\text{-}CreER}$ mice compared to controls. This finding was consistent with IGFBP1 regulation by insulin, but the fold increase was markedly above IGFBP1 levels observed during starvation (*25*). Similar observations were made in WAT (Fig. 3J). Low circulating levels of IGF-1 and IGFBP1 evoked liver degradation (Fig. 3K). However, we did not observe any evidence of endoplasmic reticulum stress (fig. S8A) or an increase in liver ubiquitination (fig. S8B), which suggests that there were other mechanisms of IGF-1/IGFBP1 degradation.

PIK3CA gain-of-function mutation in adipose tissue recruits AKT, which addresses GLUT4 at the cell membrane and allows permanent cell glucose entry and subsequent hypoglycemia. The latter reduces insulin secretion, which, in turn, markedly increases IGFBP1 production followed by liver IGF-1 sequestration and a reduction in IGF-1 circulating levels. The *PIK3CA*$^{Adipo\text{-}CreER}$ mouse model recapitulates endocrinologic disorders observed in patients.

PIK3CA gain-of-function mutation in adipose tissue induces metabolomic reprogramming

An increase in glucose uptake to favor cell growth and proliferation is a hallmark of cancer cells (*26*). We therefore explored whether *PIK3CA* gain-of-function mutations in our model were associated with metabolic switches, such as those observed in cancer (*27*, *28*). We first explored in vitro the metabolic changes associated with *PIK3CA* mutation in fibroblasts derived from *PIK3CA*$^{CAGG\text{-}CreER}$ and control mice. In normoglycemic conditions (5 mM glucose), we observed that fibroblasts derived from *PIK3CA*$^{CAGG\text{-}CreER}$ mice demonstrated a moderate increase in glycolysis, lactate production, and nicotinamide adenine dinucleotide (NAD^+) production compared to *PIK3CA*^{WT} (fig. S9, A and B). However, when mutant fibroblasts were placed in low-glucose conditions (<1 mM glucose), such as in our mouse model, we observed a major shift toward glycolysis with lactate production (Fig. 4A and figs. S10 and S11). *PIK3CA* mutant fibroblasts were associated with not only a significant increase in several tricarboxylic acid cycle intermediates, such as citrate, *cis*-aconitate, or succinate, with aerobic lactate production but also a significant increase in nicotinamide and nicotinamide-*N*-oxide, which are precursors of the oxidized form of NAD^+ (NAD) and nicotinamide adenine dinucleotide phosphate. NAD and its reduced form (NADH) were increased (Fig. 4A and fig. S10 and S11), although the change was not significant. The expression of other markers of mitochondrial respiration, such as flavin adenine dinucleotide (an electron carrier) and its precursor, riboflavin, was also elevated (Fig. 4A and figs. S10 and S11).

In addition, aerobic glycolysis was associated with anabolic pathways, as assessed by the important accumulation of essential (leucine, isoleucine, lysine, threonine, phenylalanine, methionine, histidine, and tryptophan) and nonessential (arginine and tyrosine) amino acids and the increase in fatty acid products such as myristic acid, palmitoleic acid, arachidonic acid, eicosapentaenoic acid, docosahexaenoic acid, butyric acid, or linoleic acid and carnitine consumption (Fig. 4A and figs. S10 and S11). Together, these data suggest that the *PIK3CA* construct that we used was sufficient to induce Warburg-like effect with the biosynthesis of macromolecules in fibroblasts. We next speculated whether these findings could be verified in *PIK3CA*$^{Adipo\text{-}CreER}$ mice. Plasma from 12-hour-fasted *PIK3CA*^{WT} and *PIK3CA*$^{Adipo\text{-}CreER}$ mice was then collected and processed for metabolomic analysis. Plasma derived from *PIK3CA*$^{Adipo\text{-}CreER}$ mice showed lactate production with increased levels of nicotinamide *N*-oxide and riboflavin, both of which are involved in mitochondrial respiration, compared to controls (Fig. 4B and figs. S12 and S13A). Similar to *PIK3CA* mutant fibroblasts, we observed activation of anabolic pathways with amino acid accumulation (leucine, isoleucine, lysine, oxoadipate and its metabolism intermediates, acetyl-lysine, phenylalanine, thymidine, tyrosine, valine, hydroxy-L-proline, arginine, and ornithine, its subsequent metabolite that, in turn, will lead to citrulline) or consumption (tryptophan; Fig. 4B and figs. S12 and S13A). We also noticed that the methionine/cysteine pathway was altered and the profound modification of several metabolites and enzymes involved in their metabolism, such as betaine, L-sarcosine, pyridoxal, cysteine sulfonic acid, *S*-adenosyl-L-homocysteine, and cystathionine (Fig. 4B and figs. S12 and 13). Aside from protein synthesis, several metabolites involved in ribo- and deoxyribonucleic acid synthesis, such as 5-methylcytosine and cytidine, were significantly elevated, which evokes nucleotide biosynthesis (Fig. 4B and fig. S12 and S13A). Fatty acid metabolism (decanoic acid, ac arachidonic, eicosapentaenoic acid, aminoadipate, dodecanoic acid/lauric acid, linoleic acid, linolenic acid, oleic acid, and palmitic acid) was also profoundly affected in *PIK3CA*$^{Adipo\text{-}CreER}$ mice, which is evidence of lipid synthesis (Fig. 4B and figs. S12 and S13A). Thus, plasma derived from *PIK3CA*$^{Adipo\text{-}CreER}$ mice showed metabolic evidence of aerobic glycolysis with activated anabolic pathways. Next, we decided to explore pyruvate kinase M2 (PKM2) expression in WAT of the different mouse models. PKM2 is a limiting glycolytic enzyme that catalyzes the final step in glycolysis and plays a pivotal role in the metabolic

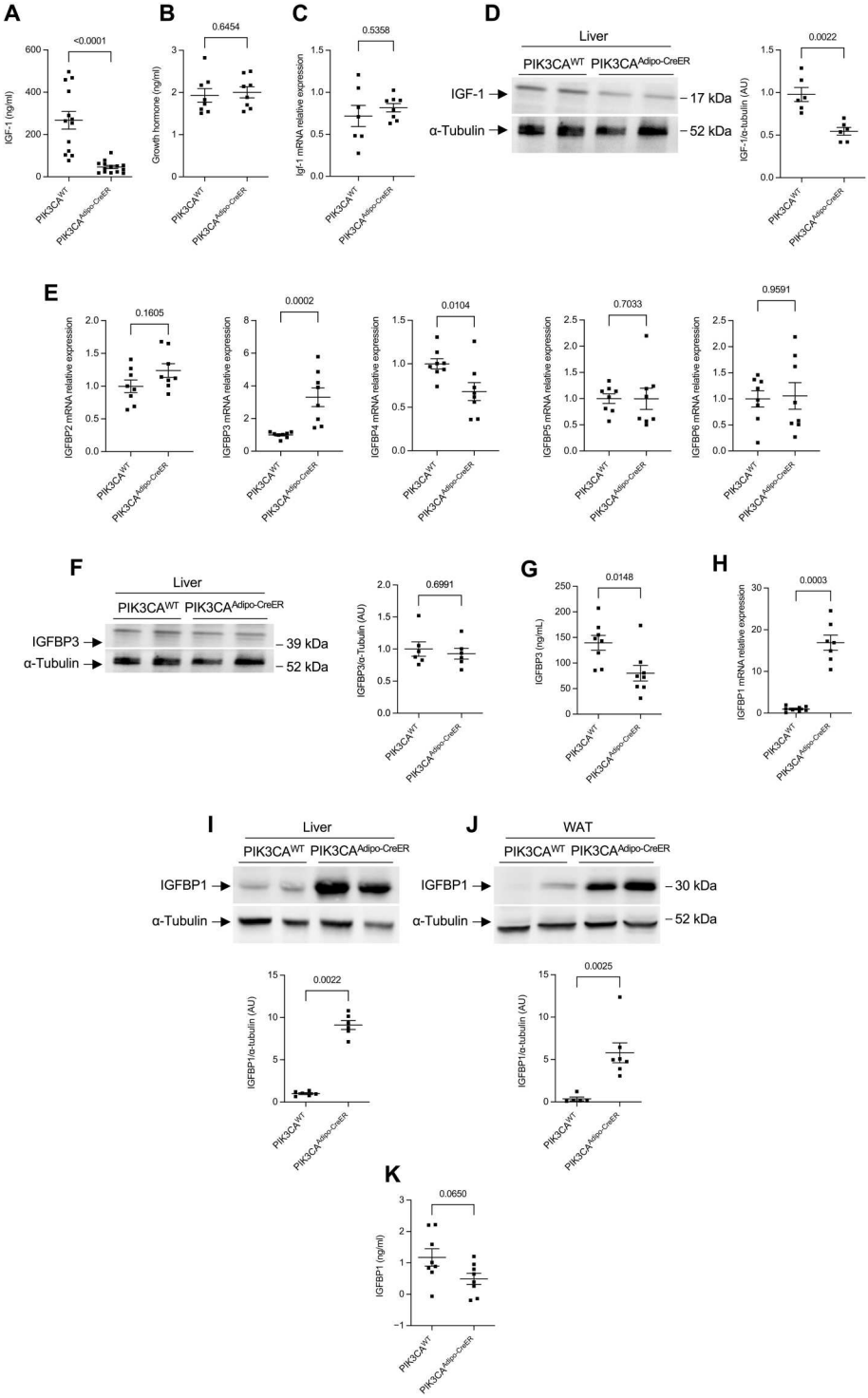

Fig. 3. *PIK3CA*$^{Adipo\text{-}CreER}$ mice present with severe endocrine disruption. (**A**) Circulating IGF-1 levels in *PIK3CA*^{WT} ($n = 13$) and *PIK3CA*$^{Adipo\text{-}CreER}$ mice ($n = 14$). (**B**) Growth hormone circulating levels in *PIK3CA*^{WT} and *PIK3CA*$^{Adipo\text{-}CreER}$ mice ($n = 8$ per group). (**C**) IGF-1 mRNA expression in the livers of *PIK3CA*^{WT} ($n = 8$) and *PIK3CA*$^{Adipo\text{-}CreER}$ mice ($n = 7$). (**D**) Western blot and quantification of IGF-1 in the livers of *PIK3CA*^{WT} and *PIK3CA*$^{Adipo\text{-}CreER}$ mice ($n = 6$ per group). (**E**) *IGFBP2* to *IGFBP6* mRNA expression in the livers of *PIK3CA*^{WT} and *PIK3CA*$^{Adipo\text{-}CreER}$ mice ($n = 8$ per group). (**F**) Western blot and quantification of IGFBP3 in the livers of *PIK3CA*^{WT} and *PIK3CA*$^{Adipo\text{-}CreER}$ mice ($n = 6$ per group). (**G**) Circulating IGFBP3 levels in *PIK3CA*^{WT} and *PIK3CA*$^{Adipo\text{-}CreER}$ mice ($n = 6$ per group). (**H**) IGFBP1 mRNA expression in the livers of *PIK3CA*^{WT} and *PIK3CA*$^{Adipo\text{-}CreER}$ mice ($n = 8$ per group). (**I**) Western blot and quantification of IGFBP1 in the livers of *PIK3CA*^{WT} and *PIK3CA*$^{Adipo\text{-}CreER}$ mice ($n = 6$ per group). (**J**) Western blot and quantification of IGFBP1 in WAT of *PIK3CA*^{WT} ($n = 5$) and *PIK3CA*$^{Adipo\text{-}CreER}$ mice ($n = 7$). (**K**) Circulating IGFBP1 levels in *PIK3CA*^{WT} and *PIK3CA*$^{Adipo\text{-}CreER}$ mice ($n = 8$ per group).

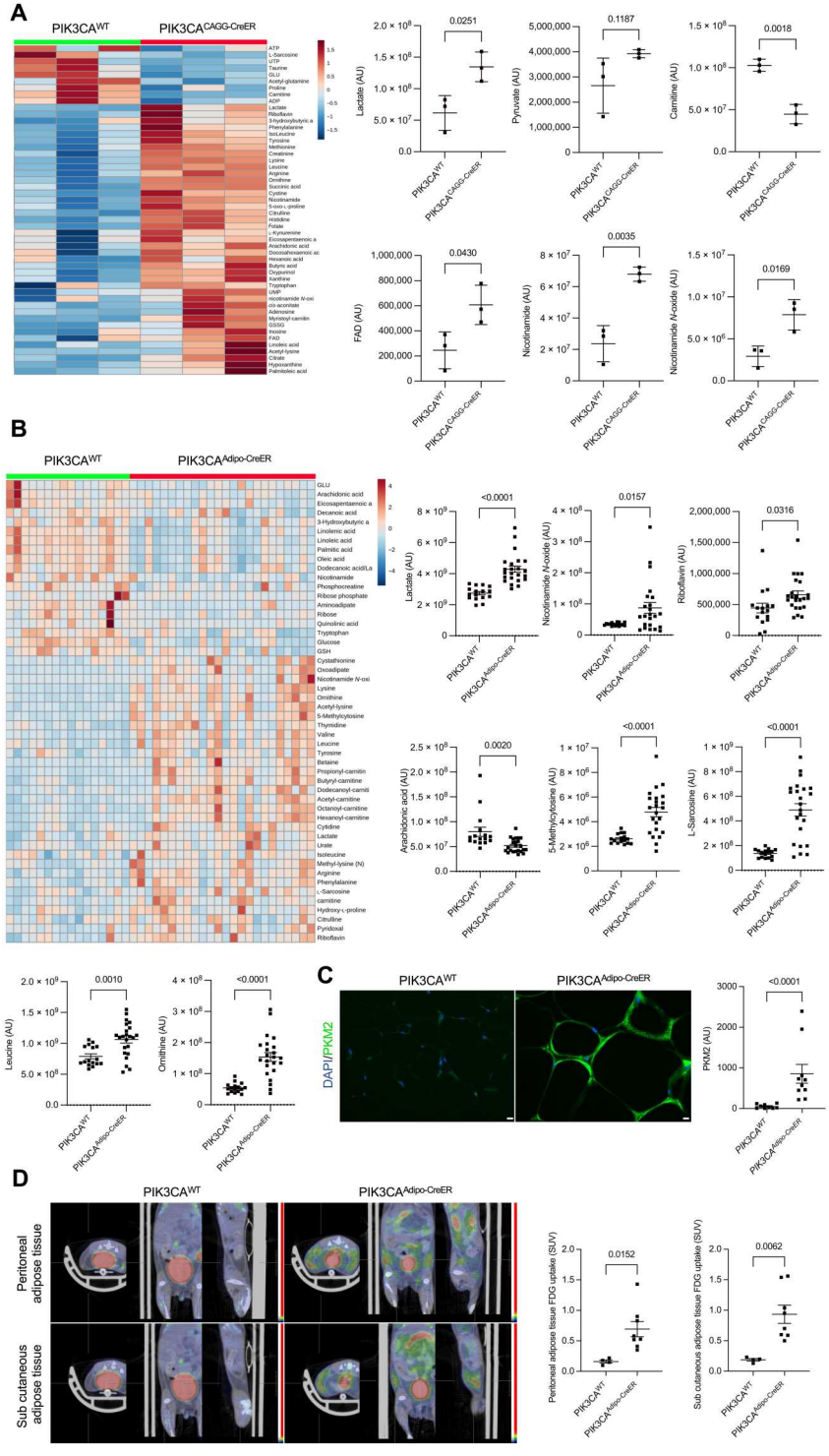

Fig. 4. *PIK3CA* gain-of-function mutation is associated in vitro and in vivo with aerobic glycolysis, lactate production, and macromolecule synthesis. (**A**) Heatmap of the 50 top metabolite changes observed in *PIK3CA*^{WT} and *PIK3CA*$^{CAGG\text{-}CreER}$ fibroblasts (n = 3 per condition) cultured in low-glucose conditions. Graphic example of metabolite modification observed. (**B**) Heatmap of the 50 top metabolite changes observed in the plasma of *PIK3CA*^{WT} (n = 16) and *PIK3CA*$^{Adipo\text{-}CreER}$ mice (n = 24). Graphic example of metabolite modification observed. (**C**) Representative immunofluorescence of PKM2 expression in WAT of *PIK3CA*^{WT} and *PIK3CA*$^{Adipo\text{-}CreER}$ mice. Scale bar, 10 μm. (**D**) 18F-fluorodeoxyglucose uptake in WAT of *PIK3CA*^{WT} (n = 4) and *PIK3CA*$^{Adipo\text{-}CreER}$ mice (n = 8).

switch observed in cancer cells (*15*). Whereas PKM2 expression was barely detectable in $PIK3CA^{WT}$ mice, its expression was significantly increased in $PIK3CA^{Adipo\text{-}CreER}$ mice (Fig. 4C). PKM2 can be detected in tissues with high-rate turnover including macrophages and when Warburg effect is activated. Coimmunostaining revealed that PKM2 was mainly expressed in adipocytes and not in F4/80-positive cells (fig. S13B). Last, to confirm the metabolic switch observed in $PIK3CA^{Adipo\text{-}CreER}$ mice, we performed 2′-deoxy-2′-[18F]fluoro-D-glucose (FDG) uptake. We consistently observed a significant increase in WAT FDG uptake in $PIK3CA^{Adipo\text{-}CreER}$ mice similar to that in patients with PROS (*17*), thus demonstrating a Warburg-like effect (Fig. 4D and fig. S13C). Last, FDG uptake was reduced in skeletal muscles of $PIK3CA^{Adipo\text{-}CreER}$ mice compared to controls, consistently with low levels of circulating insulin (fig. S13D).

PIK3CA gain-of-function mutations in adipose tissue partially signal through AKT2

In mammals, three distinct genes encode *AKT* homologs—*AKT1*, *AKT2*, and *AKT3*—and *AKT2* is known to be the main isoform in WAT and BAT (*21*). $AKT2^{-/-}$ mice (referred thereafter as $AKT2^{ko}$) have mild growth deficiency, progressive lipoatrophy, and altered glucose homeostasis with moderated hyperglycemia and hyperinsulinemia, which progressively leads to β islet failure (*21*). We next sought to investigate whether *PIK3CA* gain-of-function mutations were signaling mainly through AKT or other downstream targets. To answer this question, we interbred $AKT2^{ko}$ mice with $PIK3CA^{Adipo\text{-}CreER}$ animals to obtain $PIK3CA^{Adipo\text{-}CreER\text{-}Akt2ko}$ mice (henceforth $PIK3CA^{Akt2ko}$).

$PIK3CA^{Akt2ko}$ mice were indistinguishable from other mice for the first 6 weeks. At the age of 6 weeks, mice were given a daily dose of tamoxifen (40 mg kg^{-1}) for 5 days to induce *Cre* recombination. Following *Cre* induction, $PIK3CA^{Adipo\text{-}CreER}$ mice gained excessive weight, but the body weights of $PIK3CA^{Akt2ko}$ mice did not differ from those of $PIK3CA^{WT}$ control littermates (Fig. 5A and fig. S14A). At 13 weeks after tamoxifen administration (i.e., at 19 weeks of age), MRI showed no excess of subcutaneous and perivisceral adipose tissue in $PIK3CA^{Akt2ko}$ mice (Fig. 5B). Mice were then euthanized, and necropsy examination confirmed that $PIK3CA^{Akt2ko}$ mice were indistinguishable from control littermates. Mice had no excess adipose tissue, partial correction in organ weights (fig. S14B), and F4/80 $CD11b^+$ cell WAT infiltration (fig. S14C). Deletion of *AKT2* was associated with a complete correction of hemoglobin and white blood cell anomalies (fig. S14D). Histological examination showed that the adipocyte size of $PIK3CA^{Akt2ko}$ mice was partially rescued compared to that of $PIK3CA^{Adipo\text{-}CreER}$ mice (Fig. 5, C and D, and fig. S14E). AKT and S6RP phosphorylation in the WAT of $PIK3CA^{Akt2ko}$ mice was only partially blunted compared to that of $PIK3CA^{Adipo\text{-}CreER}$ mice (Fig. 5E). We confirmed that *AKT2* deletion was not associated with p110* expression in $PIK3CA^{Akt2ko}$ mice (fig. S14F). Although fasting glycemia was higher in $PIK3CA^{Akt2ko}$ than in $PIK3CA^{Adipo\text{-}CreER}$ mice, blood glucose levels remained lower than those of controls (Fig. 5F). The glucose tolerance test showed a peak of glycemia in $PIK3CA^{Akt2ko}$ mice superposable to control mice at 15 min, followed by a rapid decline in glycemia (fig. S15A). We then checked GLUT4 expression and observed persistent expression at the adipocyte cell membrane in $PIK3CA^{Akt2ko}$ mice (fig. S15B). GLUT4 expression has already been shown to be unaffected in $AKT2^{-/-}$ mice (*21*). Consistent with GLUT4 cell membrane expression, circulating levels of insulin (Fig. 5G) and NEFA (Fig. 5H), adiponectin expression in WAT (Fig. 5I), circulating levels of IGF-1 (Fig. 5J), IGF1 mRNA liver expression (fig. S15C), and *IGFBP1* mRNA in the liver (Fig. 5K and fig. S15D) were very partially corrected.

We then explored the metabolomic consequences of *AKT2* deletion in our model. Analysis of the sera derived from $PIK3CA^{Akt2ko}$ mice showed partial correction of several metabolic anomalies, such as lactate production, carnitine and its derivatives (butyryl carnitine, hexanoyl carnitine, and octanoyl carnitine) and nicotinamide *N*-oxide production (both of which are involved in mitochondrial respiration), reduction in amino acid levels (arginine, acetyl lysine, methyl lysine, phenylalanine, thymidine, or valine), and the methionine/cysteine pathway (betaine, L-sarcosine, ornithine, or pyridoxal; figs. S15E and S16). Consistently, we observed a partial correction in the level of PKM2 expression in WAT of $PIK3CA^{Akt2ko}$ mice (fig. S17A).

We interbred mice to ultimately obtain $PIK3CA^{HO}$ deleted for AKT2 (henceforth $PIK3CA^{HO\ Akt2ko}$). We observed that *AKT2* deletion extended the survival of $PIK3CA^{HO}$ mice (fig. S17B). We concluded that the adipose tissue overgrowth observed in $PIK3CA^{Adipo\text{-}CreER}$ mice is driven through AKT2, but because *AKT2* deletion did not correct GLUT4 accumulation at the cell membrane or endocrine disorders, it appears likely that these events are regulated through compensatory activation of AKT1 or other branches.

Impact of alpelisib on the mouse model

We recently identified alpelisib (BYL719), a PIK3CA inhibitor, as a promising therapeutic option for patients with PROS (*14*). We decided to test whether this molecule was efficient at improving adipose tissue overgrowth in our mouse model. To this end, we used two different approaches. We first administered alpelisib daily starting 48 hours after *Cre* induction to perform a preventive study. We observed that alpelisib-treated $PIK3CA^{Adipo\text{-}CreER}$ mice had an overtly normal appearance during the 6 weeks of treatment and a body weight increase similar to that of control mice (Fig. 6A). MRI performed 6 weeks after introduction of alpelisib treatment showed no adipose tissue overgrowth (Fig. 6B). Mice were then euthanized, and necropsy examination confirmed that alpelisib-treated $PIK3CA^{Adipo\text{-}CreER}$ mice had no excess adipose tissue, but organ weights were only partially restored (fig. S18A). Histology analysis showed that alpelisib-treated $PIK3CA^{Adipo\text{-}CreER}$ mice had adipocytes of intermediate size compared to $PIK3CA^{WT}$ (Fig. 6, C and D) with persistent F4/80^+CD11b^+ cell infiltration (fig. S18B). Biologically, hemoglobin and white blood cell counts were not modified by alpelisib (fig. S18C). Twelve-hour fasting glycemia was not corrected (Fig. 6E) nor were circulating insulin and IGF-1 levels (Fig. 6, F and G).

Next, we administered alpelisib to $PIK3CA^{Adipo\text{-}CreER}$ mice 6 weeks after *Cre* induction when adipose tissue was already prominent for six additional weeks as a therapeutic study. Following alpelisib introduction, we noticed a rapid body weight decrease in alpelisib-treated $PIK3CA^{Adipo\text{-}CreER}$ mice (Fig. 6A). T2-weighted magnetic resonance images performed 7 weeks after the start of treatment (i.e., 12 weeks after *Cre* induction) did not reveal the presence of adipose tissue overgrowth (Fig. 6B). Organ weights were again partially corrected (fig. S18A), and we noticed a partial recovery in the size of adipocytes (Fig. 6, C and D). F4/80^+CD11b^+ cell infiltration in WAT was still persistent (fig. S18B). Similar to the

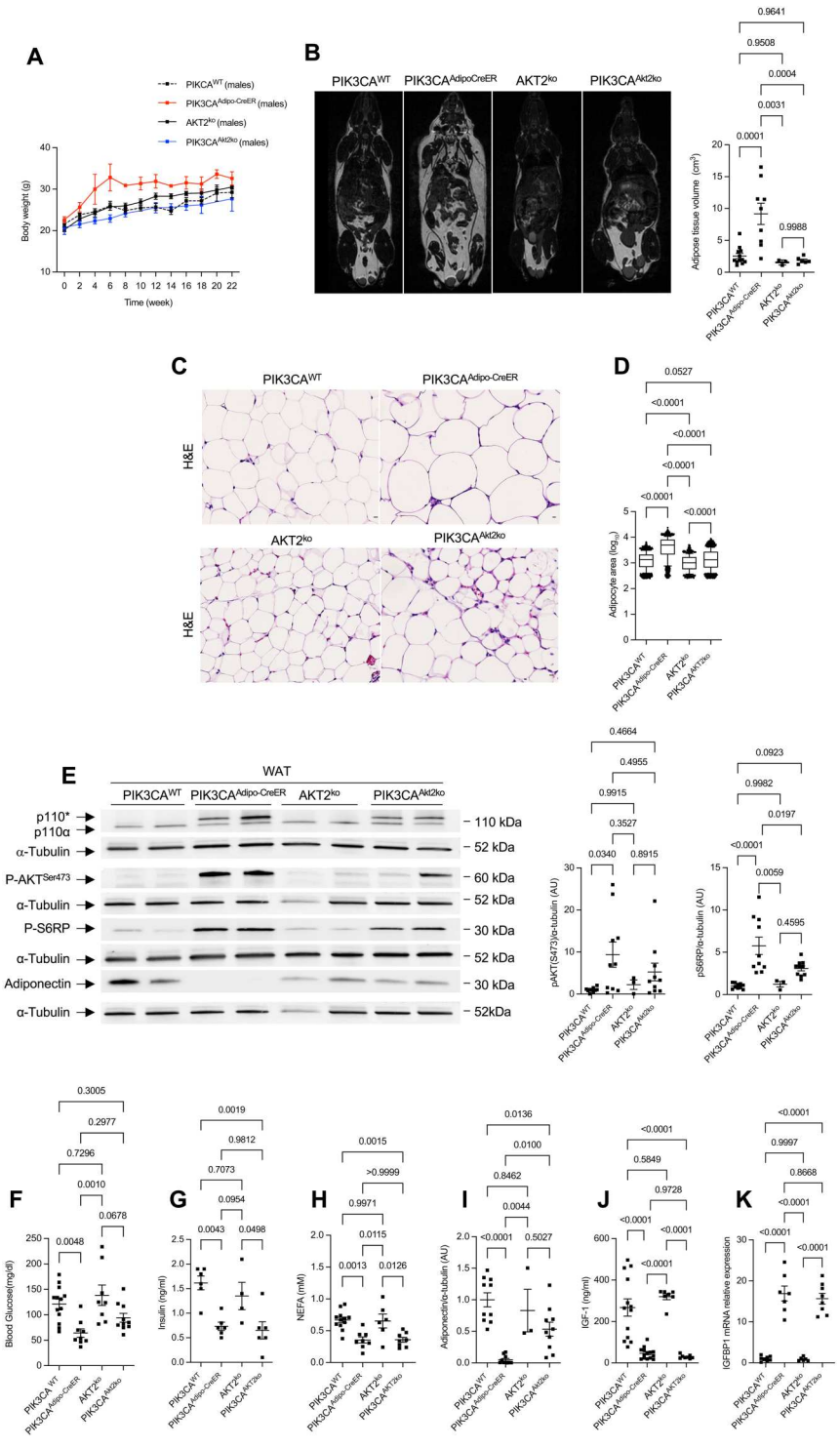

Fig. 5. *PIK3CA*$^{Adipo\text{-}CreER}$ mainly signals through AKT2. (**A**) Male body weights of *PIK3CA*^{WT}, *AKT2*^{ko}, *PIK3CA*$^{Adipo\text{-}CreER}$, and *PIK3CA*^{Akt2ko} mice (n = 15 per group) following *Cre* recombination. (**B**) Coronal whole-body T2-weighted MRIs of *PIK3CA*^{WT} (n = 12), *AKT2*^{ko} (n = 3), *PIK3CA*$^{Adipo\text{-}CreER}$ mice (n = 9), and *PIK3CA*^{Akt2ko} (n = 6) mice. Adipose tissue volume quantification. (**C**) Representative H&E staining of WAT of *PIK3CA*^{WT}, *AKT2*^{ko}, *PIK3CA*$^{Adipo\text{-}CreER}$, and *PIK3CA*^{Akt2ko} mice. Scale bar, 10 μm. (**D**) Quantification of adipocyte cell area of *PIK3CA*^{WT}, *AKT2*^{ko}, *PIK3CA*$^{Adipo\text{-}CreER}$, and *PIK3CA*^{Akt2ko} mice (n = 5 mice per group). (**E**) Western blot and quantification of p110; P-AKT^{ser473}; P-S6RP; and adiponectin in WAT of *PIK3CA*^{WT} (n = 9), *AKT2*^{ko} (n = 3), *PIK3CA*$^{Adipo\text{-}CreER}$ (n = 9), and *PIK3CA*^{Akt2ko} (n = 10) mice. (**F**) Twelve-hour fasted glycemia in *PIK3CA*^{WT} (n = 13), *AKT2*^{ko} (n = 8), *PIK3CA*$^{Adipo\text{-}CreER}$ mice (n = 9), and *PIK3CA*^{Akt2ko} (n = 10) mice. (**G**) Insulin circulating levels in *PIK3CA*^{WT} (n = 8), *AKT2*^{ko} (n = 4), *PIK3CA*$^{Adipo\text{-}CreER}$ (n = 7), and *PIK3CA*^{Akt2ko} (n = 6) mice. (**H**) NEFA circulating levels in *PIK3CA*^{WT} (n = 12), *AKT2*^{ko} (n = 8), *PIK3CA*$^{Adipo\text{-}CreER}$ (n = 8), and *PIK3CA*^{Akt2ko} (n = 8) mice. (**I**) Western blot quantification of adiponectin in WAT of *PIK3CA*^{WT} (n = 9), *AKT2*^{ko} (n = 3), *PIK3CA*$^{Adipo\text{-}CreER}$ (n = 9), and *PIK3CA*^{Akt2ko} (n = 10) mice. (**J**) Circulating IGF-1 levels in *PIK3CA*^{WT} (n = 13), *AKT2*^{ko} (n = 6), *PIK3CA*$^{Adipo\text{-}CreER}$ (n = 14), and *PIK3CA*^{Akt2ko} (n = 8) mice. (**K**) IGFBP1 mRNA expression in the livers of *PIK3CA*^{WT}, *PIK3CA*$^{Adipo\text{-}CreER}$, and *PIK3CA*^{Akt2ko} mice (n = 6 to 8 per group).

alpelisib preventive study, blood cell counts were not ameliorated (fig. S18C), and glycemia partially improved after 12 hours of fasting (Fig. 6E). This was consistent with partial rescue of glucose uptake in vitro (fig. S18D).

Both schemes of alpelisib administration were associated with macroscopic improvement of adipose tissue overgrowth, but persistent hypoglycemia and endocrine anomalies were less pronounced in the therapeutic scheme (Fig. 6, F to H). To better decipher the discrepancy between the preventive and therapeutic protocols, we first explored the phosphorylation of AKT and S6RP in WAT at different time points following alpelisib gavage. We observed that phosphorylation of the two proteins was blunted 1.5 hours after alpelisib administration and returned to higher values very quickly afterward (fig. S18E). A peak in glycemia was consistently observed

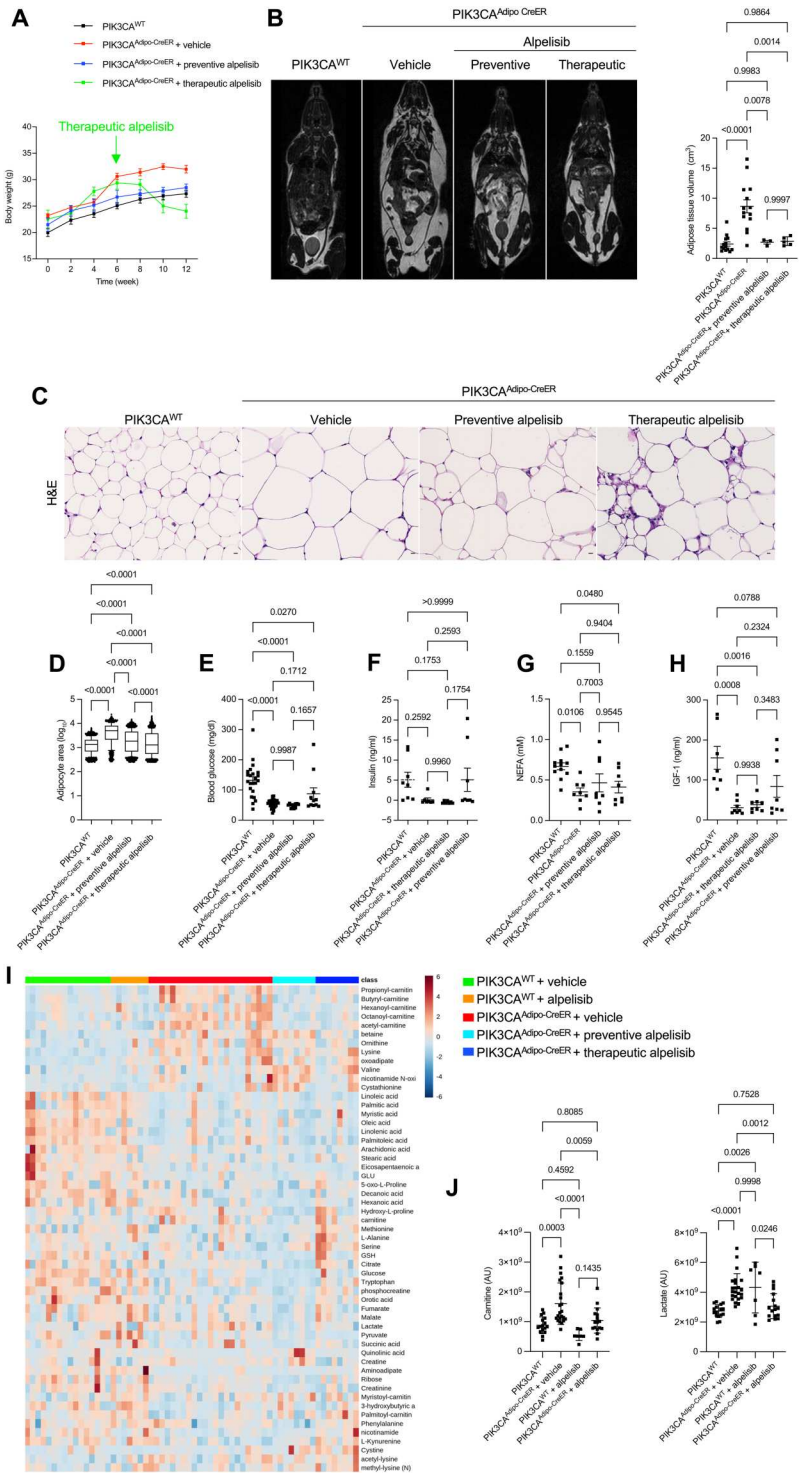

Fig. 6. Alpelisib prevents and reverses adipose tissue overgrowth in *PIK3CA*$^{Adipo\text{-}CreER}$ mice and only partially corrects endocrine disruption. (**A**) Male body weights of *PIK3CA*^{WT} (n = 14) and *PIK3CA*$^{Adipo\text{-}CreER}$ treated with either vehicle (n = 14), preventive (n = 3), or curative alpelisib (n = 5). (**B**) Whole-body T2-weighted MRIs of *PIK3CA*^{WT} (n = 14), *PIK3CA*$^{Adipo\text{-}CreER}$ vehicle-treated (n = 14), *PIK3CA*$^{Adipo\text{-}CreER}$-treated with preventive alpelisib (n = 3), and *PIK3CA*$^{Adipo\text{-}CreER}$-treated with therapeutic alpelisib (n = 5) mice. Adipose tissue volume quantification. (**C**) Representative H&E staining of WAT of *PIK3CA*^{WT} and *PIK3CA*$^{Adipo\text{-}CreER}$ mice treated with either vehicle, preventive, or curative alpelisib. Scale bar, 10 μm. (**D**) Adipocyte cells surface of *PIK3CA*^{WT} and *PIK3CA*$^{Adipo\text{-}CreER}$ mice treated with vehicle, preventive, or curative alpelisib (n = 5 per group). (**E**) Twelve-hour fasted glycemia in *PIK3CA*^{WT} (n = 23) and *PIK3CA*$^{Adipo\text{-}CreER}$ mice treated with vehicle (n = 23), preventive (n = 12), or curative (n = 11) alpelisib. (**F**) Insulin circulating levels in *PIK3CA*^{WT} (n = 8) and *PIK3CA*$^{Adipo\text{-}CreER}$ mice treated with either vehicle (n = 8), preventive (n = 8), or curative (n = 8) alpelisib. (**G**) NEFA circulating levels in *PIK3CA*^{WT} (n = 12) and *PIK3CA*$^{Adipo\text{-}CreER}$ mice treated with either vehicle (n = 8), preventive (n = 8), or curative (n = 8) alpelisib. (**H**) Circulating IGF-1 levels in *PIK3CA*^{WT} (n = 7) and *PIK3CA*$^{Adipo\text{-}CreER}$ mice treated with vehicle (n = 8), preventive (n = 8), or curative (n = 8) alpelisib. (**I**) Heatmap of the 55 top metabolite changes observed in the plasma from *PIK3CA*^{WT} (n = 16), *PIK3CA*^{WT} treated with alpelisib (n = 7), and *PIK3CA*$^{Adipo\text{-}CreER}$ mice treated with vehicle (n = 24), preventive (n = 8), or curative (n = 8) alpelisib. (**J**) Graphic example of metabolite modification observed.

approximately 1 hour following alpelisib, which thereafter quickly returned to lower values (fig. S18F). The kinetics of glycemia in *PIK3CA*$^{Adipo\text{-}CreER}$-starved mice following alpelisib administration was different between the treatment schemes (fig. S18F). Blood glycemia rapidly returned to lower values in the preventive group following alpelisib administration, while glycemia improvement was more sustained in the therapeutic protocol. This suggests that the half-life of alpelisib in adipose tissue is relatively short and more sustained when alpelisib is introduced after the disease is already installed. Alpelisib measurement in WAT supported these findings with an increased accumulation of drug in mice of the therapeutic protocol (fig. S18G). This was consistent with lipophilic affinity of alpelisib.

Consistent with what was observed in *PIK3CA*$^{Adipo\text{-}CreER}$ fibroblasts exposed to alpelisib (fig. S19A), pooled analysis of the sera derived from mutant mice treated with alpelisib was associated with a complete or partial rescue of different metabolites, such as lactates, carnitine and its derivatives (hexanoyl carnitine and octanoyl carnitine), and cytidine (a nucleoside molecule), less accumulation of amino acids such as thymidine and L-sarcosine, and a reduction of pyridoxal (which is involved in the methionine/cysteine pathway) and quinolinic acid (which participates in NAD formation and mitochondrial respiration; Fig. 6, I and J). Alpelisib was able to correct aerobic glycolysis and reduce the activity of anabolic pathways.

Last, we treated *PIK3CA*^{HO} with alpelisib and observed extension of mouse survival (fig. S19B). We concluded that alpelisib improves *PIK3CA*$^{Adipo\text{-}CreER}$ mice and may represent a promising therapeutic for patients with *PIK3CA*-related adipose tissue overgrowth.

Patients with PIK3CA-related adipose tissue overgrowth

Adipose tissue overgrowth is a common observation in patients with PROS. We decided to test whether our findings were relevant to patients. Among our cohort, we identified 12 patients with PROS (Table 1) mainly affected by adipose tissue overgrowth who were treated with alpelisib for at least 6 months. We first performed P-AKT^{T308}, P-S6RP, leptin, and GLUT4 immunostaining in skin biopsies from three controls (healthy skin removed during surgical procedures) and six patients with *PIK3CA*-related adipose tissue overgrowth before alpelisib introduction. Immunofluorescence revealed adipose tissue disorganization with detectable AKT and S6RP phosphorylation in affected patients compared to controls (Fig. 7, A and B, and fig. S20A). We observed linear GLUT4 accumulation at the cell membrane of adipocytes, as was the case in the *PIK3CA*$^{Adipo\text{-}CreER}$ mouse model, compared to granular cytoplasmic staining in controls (Fig. 7C). PKM2 expression was significantly increased in WAT of patients with PROS compared to controls, evocating the presence of aerobic glycolysis (Fig. 7, A and B). Biologically, we observed low circulating levels of IGF-1 in the serum of the 12 patients before alpelisib introduction that was fully corrected 6 months following drug introduction (Fig. 7D and fig. S20B). As previously observed, alpelisib was associated with clinical improvement with aesthetic changes (Fig. 7E and fig. S20C). Adipose tissue malformation was accessible to volume measurement using MRI in seven patients (Table 1). MRI showed a decrease in the mean preselected malformation volume from 3437 cm^3 (interquartile range, 183 to 14, 254) before alpelisib introduction to 2372 cm^3 (interquartile range, 155 to 9774) over 6 months on alpelisib [mean (SD) change, −22.54 (9.9)%] (Fig. 7, F and G; fig. S20D; and Table 1).

Last, we explored the metabolomic changes before and after alpelisib introduction in this unique cohort. As observed first in vitro and then in vivo, we found important changes in several serum metabolites.

Alpelisib was associated with a reduction in circulating lactate and pyruvate levels and a decrease in the levels of several metabolite intermediates of mitochondrial respiration (carnitine and several metabolites and nicotinamide *n*-oxide), amino acids (acetyl lysine, glycine, hydroxy-L-proline, and tryptophan), tricarboxylic acid cycle intermediates (arginiosuccinate and *cis*-aconitate), and methionine/cysteine pathway changes (betaine; Fig. 7H and figs. S20E and S22). Thus, plasma derived from patients treated with alpelisib showed metabolic evidence of aerobic glycolysis and anabolic pathway modifications 6 months after drug introduction.

DISCUSSION

For the present study, we created a mouse model of *PIK3CA* gain-of-function mutations in adipose tissue. This model recapitulates the phenotype of a subgroup of patients with PROS and their specific metabolic anomalies, including hypoglycemia with low circulating levels of insulin and IGF-1. We deciphered the mechanism of chronic hypoglycemia observed in this population and demonstrated that these anomalies were mainly driven through AKT2. We showed the efficacy of alpelisib in a mouse model and then confirmed these data in patients. Last, we showed that isolated *PIK3CA* gain-of-function mutations are associated, in preclinical models and in patients, with Warburg-like effect and a biosynthesis of macromolecules similar to that in cancer cells.

PIK3CA$^{Adipo\text{-}CreER}$ mice showed anatomical and histological adipose tissue overgrowth similar to that observed in patients with PROS. However, it is important to note that this mouse model has several caveats. First, we induced PIK3CA overactivation in already differentiated adipocytes. Second, we used a transgene that does not exist in human but is extremely powerful (*29*). Third, we did not use a knock-in approach but instead added the transgene at the Rosa26 locus, creating a mouse with three *PIK3CA* alleles. However, this mouse model is the first that recapitulates disease phenotype observed in patients with *PIK3CA*-related adipose tissue overgrowth including hormonal anomalies observed in this group of patients. Other groups have explored the impact of specific overaction of the PI3K pathway in adipose tissue, but our model robustly reproduces the patient phenotype. *PTEN* deletion in mouse adipose tissue does not induce adipose tissue overgrowth (*29*). These mice have normal circulating adiponectin levels and basal hypoinsulinemia but do not exhibit hypoglycemia and have increased GLUT4 cell membrane expression (*29*). *TSC1* deletion in adipocytes induces mTOR overactivation but is associated with reduced perivisceral adipose tissue (*30*). We also found that most of the phenotype was driven through AKT2, and patients with *AKT2* gain of function present with metabolic and hormonal anomalies similar to those of *PIK3CA*$^{Adipo\text{-}CreER}$ mice (*31*, *32*). GLUT4 expression was not modulated in *PIK3CA*^{Akt2ko} mice, suggesting that this protein is regulated by AKT1 or others such as 5' adenosine monophosphate-activated protein kinase (AMPK). This will have to be examined in further studies. We further demonstrated that alpelisib was able not only to prevent adipose tissue overgrowth development but also to reverse these anomalies during the treatment period. Patients treated with alpelisib demonstrated adipose tissue shrinkage and correction of endocrine and metabolic anomalies. Alpelisib was recently granted accelerated approval by the U.S. Food and Drug Administration for patients with PROS (>2 years old) based on real-word evidence from the EPIK P1 clinical trial (NCT04285723). Currently, a confirmatory clinical trial, EPIK P2 (NCT04589650), is ongoing. MRI follow-up of these patients will help appreciate the impact of alpelisib on the different tissues and, in particular, in adipose tissue.

The presence of *PIK3CA* mutation in adipose tissue allows cells to acquire many features of cancer cell such as increased glucose uptake, growth, Warburg effect, and macromolecules synthesis. Metabolomic changes associated with *PIK3CA* mutations were already

Table 1. Patient characteristics. VAF, variant allele frequency, corresponds to the percentage of alternate or mutant reads to total reads detected by next generation sequencing; COSMIC, Catalogue of Somatic Mutations in Cancer; NA, not available.

	Patient 1	Patient 2	Patient 3	Patient 4	Patient 5	Patient 6	Patient 7	Patient 8	Patient 9	Patient 10	Patient 11	Patient 12
Age (years)	2	2	3	5	5	10	11	15	23	27	29	49
Specimen used for genotyping	Skin	Skin	Skin	Skin	Skin	Skin	Skin	Skin	Skin	Skin	Skin	Skin
DNA changes	c.3132T>A	c.3140A>G	c.2176G>A	c.1252G>A	c.3073A>G	c.3139C>T	c.3140A>G	c.3139C>T	c.3140A>G	c.1357G>A	c.1633G>A	c.3139C>T
VAF (%)	12	8	10	27	7	32	8	12	12	5	8	10
Amino acid change	p.N1044K	p.H1047R	p.E726K	p.E418K	p.T1025A	p.H1047Y	p.H1047R	p.H1047Y	p.H1047R	p.E453K	E545K	p.H1047Y
COSMIC Genomic mutation ID	55897116	55873195	55875460	55880477	55873252	55876499	55873195	55876499	55873195	55874585	55873239	55876499
Alpelisib (mg per day)	50	50	50	50	50	50	50	50	250	250	250	250
Volume of the malformation (cm^3)												
Before alpelisib introduction	NA	NA	NA	NA	NA	6870	285	183	662	222	1585	14254
Six months following alpelisib introduction	NA	NA	NA	NA	NA	4640	260	155	551	175	1052	9774
Volume change following alpelisib (%)	NA	NA	NA	NA	NA	−32.4	−8.7	−15.3	−15.5	−20.9	−33.6	−31.4

assessed, but these experiments were performed only in immortalized cell lines carrying additional mutations (*33*–*37*). Our study shows, in vitro, in vivo, and in patients carrying a single *PIK3CA* gain-of-function mutation, the presence of a metabolomic switch with aerobic glycolysis, lactate production, and protein and lipid synthesis that was reversible using alpelisib. This is consistent with our previous observation, where we saw that a subgroup of patients with PROS had hypermetabolic tissues with increased FDG uptake (*17*). PIK3CA is known to control anabolic metabolism partially through AKT that recruits key effectors in cell metabolism (*38*, *39*). Supporting that, we observed that *AKT2* deletion in $PIK3CA^{Adipo\text{-}CreER}$ mice was associated with improvement of metabolomic parameters. Metabolomic anomalies were also improved with alpelisib, suggesting that these metabolites can be used to monitor drug efficacy in patients with adipose tissue overgrowth. It is intriguing that metabolic pathway alterations in adipocytes with aberrant accumulation of metabolites in the environment do not promote tumorigenesis (*40*). This suggests that *PIK3CA* mutations require additional molecular events to promote cancer cell transformation. This model offers a unique opportunity to better understand metabolic transformations induced by a single *PIK3CA* mutation and to potentially identify anticancer drugs aiming at inhibiting glycolysis (*34*, *36*, *37*, *41*, *42*). In conclusion, we deciphered the metabolic anomalies observed in patients with *PIK3CA*-adipose tissues overgrowth and demonstrated the presence of a reversible aerobic glycolysis in patients with *PIK3CA*-related adipose tissue overgrowth.

METHODS

Animals

Following procedures previously described in (*43*), we interbred homozygous *R26StopFLP110** (stock no. 012343) mice with *Adiponectin Cre-ER* mice (stock no. 025124), both obtained from the Jackson Laboratory. We obtained $R26StopFLP110^{*+/-}$ × *Adipo Cre-ER*$^{+}$ (henceforth $PIK3CA^{Adipo\text{-}CreER}$) and $R26StopFLP110^{*+/-}$ × *Adipo Cre-ER*$^{-}$ (henceforth $PIK3CA^{WT}$) mice. We also generated *Adipo Cre-ER*$^{+}$ mice with a homozygous *R26StopFLP110** mutation (henceforth $PIK3CA^{HO}$). The p110* protein expressed by *R26StopFLP110** mice is a constitutively active chimera that contains the iSH2 domain of p85 fused to the NH2 terminus of p110 via a flexible glycine linker (*44*). To generate tissue-specific p110*-transgenic mice, a cloned loxP-flanked neoR-stop cassette was inserted into a modified version of pROSA26-1, followed by cDNA encoding p110* and then an frt-flanked internal ribosomal entry site–EGFP (enhanced GFP) cassette and a bovine polyadenylation sequence (*R26StopFLP110**) (*45*). To follow *Cre* recombination, $PIK3CA^{WT}$ and $PIK3CA^{Adipo\text{-}CreER}$ mice were then interbred with $Gt(ROSA)26Sor^{tm4(ACTB\text{-}tdTomato,\text{-}EGFP)Luo/J}$ mice (*18*, *43*). These mice express a cell membrane–localized tdTomato fluorescent protein in all tissues that is replaced by GFP after *Cre* recombination.

Animals were fed ad libitum and housed at a constant ambient temperature in a 12-hour light cycle. Animals were fed with regular chow food (2018 Teklad global 18% protein rodent diets, 3.1 kcal/g; Envigo). Animal procedures were approved by the Ministère de l'Enseignement Supérieur, de la Recherche et de l'Innovation (APAFIS N°20439-2018121913526398). All appropriate procedures were followed to ensure animal welfare.

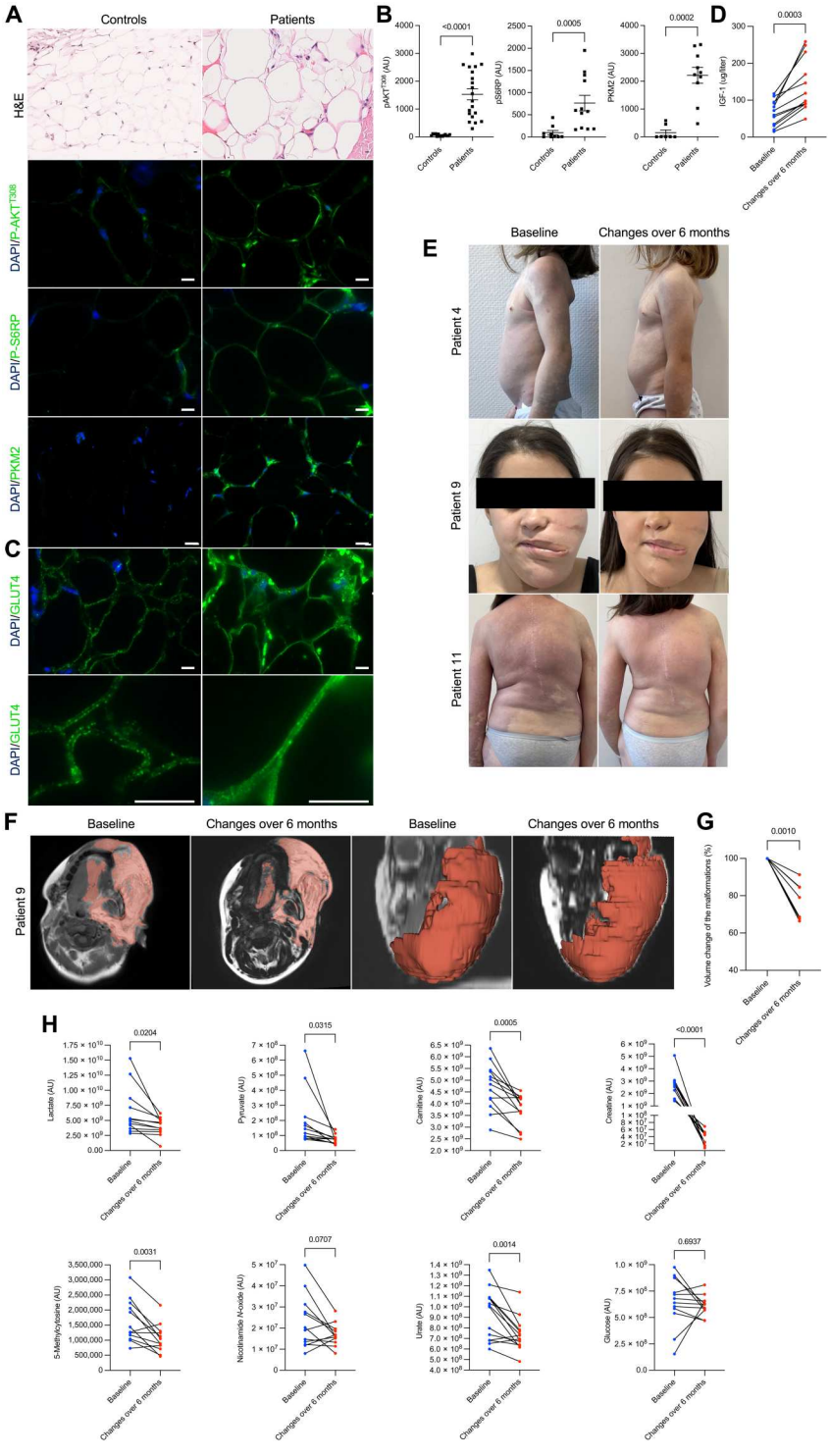

Fig. 7. Alpelisib improves adipose tissue overgrowth and metabolic changes in patients with PROS. (**A**) Representative H&E staining and immunofluorescence of P-AKT^{Ser473}, P-S6RP, and PKM2 in skin biopsies were performed in controls (n = 3) and in patients with PROS (n = 6). (**B**) Immunofluorescence quantification. (**C**) Representative GLUT4 immunofluorescence in skin biopsies performed in controls (n = 3) and in patients with PROS (n = 3). (**D**) Circulating IGF-1 levels (yellow areas highlight the normal values of the laboratory) in patients with PROS before and after alpelisib introduction (n = 12 patients). (**E**) Representative pictures of the morphological changes observed in patients with PROS receiving alpelisib for 6 months. (**F**) Transversal (left) and coronal (right) T1 face MRI of patient 9 before and after alpelisib introduction. In red, the radiologist segmentation was overlaid in 2D (left) and 3D (right). (**G**) Percentage change of the volume of the preselected lesion in seven patients. (**H**) Graphic example of metabolite changes observed in serum from patients with PROS before and after alpelisib initiation.

At the age of 6 weeks, *PIK3CA*^{WT} and *PIK3CA*$^{Adipo\text{-}CreER}$ mice received a daily dose of tamoxifen (40 mg kg^{-1}) for five consecutive days. Tamoxifen was administered through oral gavage.

PIK3CA$^{Adipo\text{-}CreER}$ mice were interbred with *AKT2*$^{-/-}$ mice obtained from the Jackson Laboratory (stock no. 006966) to generate mice with *PIK3CA* gain-of-function mutations in adipocytes but lacking *AKT2* (*PIK3CA*$^{Adipo\text{-}CreER\text{-}Akt2ko}$ mice; henceforth *PIK3CA*^{Akt2ko}).

PIK3CA^{WT} and *PIK3CA*$^{Adipo\text{-}CreER}$ mice were treated with the PIK3CA inhibitor alpelisib [MedChemExpress, Germany; 50 mg kg^{-1} in 0.5% carboxymethylcellulose (Sigma-Aldrich), daily, orally] or vehicle [0.5% carboxymethylcellulose (Sigma-Aldrich), daily, orally]. Treatment was started either 1 (preventive study) or 6 weeks (therapeutic study) following Cre induction. The last dose of alpelisib or vehicle was administered approximately 3 hours before sacrifice.

All mice were fasted for 12 hours before blood glucose measurement (Accu-Chek Performa, Roche Diagnostic), MRI, and sacrifice. A previously described *PIK3CA*$^{CAGG\text{-}CreER}$ mouse model (*17*) was used to isolate fibroblasts for metabolic in vitro experiments.

MRI evaluation

All images were acquired with a 4.7-T small-animal MRI system (Biospec USR47/40; Bruker BioSpin, Ettlingen, Germany) on the "Plateforme Imageries du Vivant, Université de Paris, PARCC, INSERM, Paris, France." Mice underwent whole-body MRI using three-dimensional (3D) T2-weighted sequences with and without fat saturation. Volumetric evaluation by MRI was performed with 3D Slicer software (*46*) and IntelliSpace Portal software (Philips Healthcare). Whole-body adipose tissue segmentation was obtained by thresholding on T2-weighted sequence and then removing hypersignal related to water on T2-weighted sequence with fat saturation. Muscles of each limb were manually segmented according to their low signal intensity and anatomy on T2-weighted sequence. For both adipose and muscle tissues, volume was calculated by summing images based on 2D contours and slice thickness.

FDG positron emission tomography–computed tomography imaging

Mice were fasted overnight with free access to water. Mice were then anesthetized (2 ± 0.5% isoflurane in dioxygen) and weighed, and glycemia was measured in blood drawn from the caudal ventral artery using an Accu-Chek Aviva Nano A (Accu-Chek, France). A 29-gauge needle catheter (Fisher Scientific, France) connected to 5-cm polyethylene tubing (0.010 inches × 0.030-inch outer diameter; Tygon Microbore Tubing, Fisher Scientific, France) was inserted into the caudal vein for radiotracer injection. FDG (9.2 ± 1.5 megabecquerel; Advanced Applied Applications, France) in 0.2-ml saline was injected via the catheter. Mice were left awake in their cage for 45 min and then installed into the positron emission tomography–computed tomography (PET-CT)–dedicated bed. Respiration and body temperature were registered. Body temperature was maintained at 34° ± 2°C, and anesthesia was controlled according to the breathing rate throughout the entire PET-CT examination. CT was acquired in a PET-CT scanner (nanoScan PET-CT; Mediso Medical Imaging Systems, Hungary) using the following acquisition parameters: semicircular mode, 50-kV tension, 720-projection full scan, 300 ms per projection, and binning of 1:4. CT projections were reconstructed by filtered retroprojection (filter, cosine; cutoff, 100%) using Nucline 3.00.010.0000 software (Mediso Medical Imaging Systems, Hungary). Fifty-five minutes after tracer injection, PET data were collected for 10 min in list mode and binned using a 5-ns time window, with a 400- to 600-keV energy window and a 1:5 coincidence mode. Data were reconstructed using the TeraTomo reconstruction engine [3D-ordered subsets expectation-maximization (OSEM)–based manufactured customized algorithm] with expectation maximization iterations, scatter, and attenuation correction. Volumes of interest (VOIs) were delineated on the organs or anatomical structure of interest on PET/CT fusion slices using the PMOD software package (PMOD Technologies Ltd., Zürich, Switzerland). FDG accumulation was quantified as the standard uptake value, which measures the ratio of the radioactivity concentration in VOI to the whole-body concentration of the injected radioactivity.

Blood and plasma analysis

At the end of each experiment, blood samples were collected from the mice in EDTA-coated tubes. To measure blood count, fresh blood samples were analyzed on a hematology analyzer (ProCyte Dx; IDEXX Laboratories) and centrifuged at 500*g* for 15 min. The collected plasma concentration was used to determine leptin (Novus Biologicals, reference no. M0B00), adiponectin (Novus Biologicals, reference no. MRP300), insulin [U-PLEX Mouse Insulin assay (Meso Scale Discovery), reference no. K1526HK], IGF-1 (Novus Biologicals, reference no. MG100), growth hormone (Ozyme, reference no. MOFI00849), β-hydroxybutyrate (Sigma-Aldrich, reference no. MAK041), and triglyceride circulating levels (Sigma-Aldrich, reference no. MAK266) using enzymatic methods from commercially available kits. NEFAs were detected with an enzymatic colorimetric assay (Fujifilm; Wako). Total cholesterol, triglycerides, and creatinine were measured by IDEXX Laboratories.

Intraperitoneal glucose and pyruvate tolerance test

Mice were fasted overnight (12 hours) with access to drinking water. All body weights were measured, and tails were carefully cut for blood glucose determination (time point 0). During glucose tolerance test, freshly prepared glucose solution was administered by intraperitoneal injection [20% glucose solution (1 g glucose/kg body weight) in water (Sigma-Aldrich, reference no. G8270)]. After 15, 30, 45, 60, 90, and 120 min, blood glucose was measured again at all time points. During pyruvate tolerance test, mice were intraperitoneally injected with sodium pyruvate (2 g/kg body weight; Sigma-Aldrich, reference no. P5280) or vehicle. After 15, 30, 45, 60, 90, and 120 min, blood glucose was measured again at all time points, and plasma were collected with Microvette CB300 (Sarstedt).

Leptin resistance test

Mice were fasted overnight, and surgical excision of the hypothalamic region was performed 30 min after intraperitoneal injection of saline or leptin (5 mg/kg; R&D, reference no. 498-OB-05M). Then, 30 μg of total protein per sample was used for Western blot analysis and hybridized with P-STAT3 and STAT3 antibodies (see below).

Energy expenditure measurements

Mice were first acclimatized to the metabolic cages and housed individually for 3 days before measurements were taken. Metabolic parameters and heat production were determined by using TSE PhenoMaster V5.3.8 (2015-5140). Food intake was determined by weighing chow food weekly for 1 month (three mice per cage for this experiment).

Morphological analysis

Mouse tissues were fixed in 4% paraformaldehyde and paraffin-embedded. Tissue sections (4 μm thick) were stained with hematoxylin and eosin (H&E). All experiments were performed in gonadal fat pads for WATs and in the interscapular region for BATs.

Measurement of adipocyte area and muscle fiber size

H&E WAT slides were scanned with a NanoZoomer 2.0-HT (Hamamatsu) and analyzed with QuPath-0.2.3 (*47*). Adipocytes were segmented using QuPath with first pixel classification (with random trees algorithm) and then QuPath object creation. Muscles were segmented using the deep learning Cellpose algorithm (*48*). For both, area was then measured with Fiji (*49*).

Immunohistochemistry and immunofluorescence

Paraffin-embedded tissue sections (4 μm) were submitted to antigen retrieval protocols using high temperature (120°C) and high pressure in citrate buffer and a pressure cooker. Sections were then incubated with primary antibodies (table S1). For the immunofluorescence procedure, appropriate Alexa Fluor–conjugated secondary antibodies (Thermo Fisher Scientific) were incubated on the samples and analyzed using an LSM 700 confocal microscope (Zeiss) or Eclipse Ni-E (Nikon). Immunohistochemistry revelation was performed with appropriate horseradish peroxidase–linked secondary antibodies and analyzed with E800 (Nikon).

In human skin biopsies, P-S6RP, P-AKT^{T308}, and PKM2 staining were segmented with Ilastik v1.3.3post3, a machine learning pixel classification open source software. For each immunofluorescence staining, mean intensity area and quantity were measured with Fiji v2.3.0/1.53f51 (quantity = mean intensity × area) and normalized by tissue (*50*).

Stochastic optical reconstruction microscopy

Paraffin-embedded WAT sections were submitted to antigen retrieval protocols using high temperature (120°C) and high pressure in citrate buffer and a pressure cooker. Sections were then incubated with GLUT4 primary antibody (table S1), and Alexa Fluor 647 antibody was incubated on samples. An oxygen-poor mounting medium was used [50% VECTASHIELD (Vector Laboratories, reference no. H1000), 30% glycerol (Sigma-Aldrich) + 2% n-Propyl gallate (Sigma-Aldrich; no. 02370), and 20% 1 M tris (pH 8)] to activate photoswitchable molecules. Acquisitions were performed using Nikon TiE and NIS-Element (Nikon), and images were reconstructed using the UNLOC plugin for ImageJ software (ImageJ, National Institutes of Health) (*51*).

mRNA analysis

mRNAs were quantified in mouse tissues by quantitative polymerase chain reaction with reverse transcriptase using CFX Connect (Bio-Rad). The primers used in this study are listed in table S2.

Western blot

Tissues were crushed and then lysed in radioimmunoprecipitation assay lysis buffer supplemented with phosphatase and protease inhibitors. Protein concentrations were determined through the bicinchoninic acid method (Pierce). Then, protein extracts were resolved by SDS–polyacrylamide gel electrophoresis before being transferred onto the appropriate membrane and incubated with the primary antibody (table S1) followed by the appropriate peroxidase-conjugated secondary antibody (dilution 1:10,000). Chemiluminescence was acquired using ChemiDoc MP, and bands were quantitated using Image Lab Software (Bio-Rad Laboratories).

Flow cytometry

To isolate bone marrow, we first dissected tibia and femur and then removed skeletal muscles, ligaments, and tendons. Cells were flushed from the marrow using 1-ml syringe containing phosphate-buffered saline (PBS) 1×. Cell suspension was centrifuged at 500*g* within 5 min and filtered (35 μm). Cells were incubated with conjugated primary antibodies (table S1). Red blood cells were lysed from blood samples (Sony; no. 2701505) and centrifuged at 500*g* within 5 min. Cells were then incubated with conjugated primary antibody (table S1). Appropriated isotype controls were used. Samples were analyzed using Sony SP6800 and Sony SP6800 software. For macrophages analysis, the pellet containing stromal/vascular cells was resuspended, and cells were labeled with conjugated primary antibody (table S1).

Adipocyte digestion

WAT of mice was rinsed in PBS 1× (Gibco) and cut into small pieces. Digestion buffer was added [1 ml/0.25 g of tissue; 2.5 mM glucose (Sigma-Aldrich, reference no. G8270), 2% fetal bovine serum (FBS), 200 μM adenosine (Sigma-Aldrich, reference no. 4036), and collagenase (1 mg/ml; Sigma-Aldrich, reference no. C2139) in Krebs-Ringer-Hepes (120 mM NaCl, 4,7 mM KCl, 2.2 mM $CaCl_2$, 10 mM Hepes, 1.2 mM KH_2PO_4, and 1.2 mM $MgSO_4$)] and incubated 1 hour at 37°C, on gentleMACS (Miltenyi). Following dissociation, WAT was filtered (150 μm; Partec GmbH), centrifuged 8 min at 150*g*, and resuspended in Hank′s balanced salt solution (HBSS1X) supplemented with 2% FBS and 200 μM adenosine. During centrifugation of digested WAT, the adipocytes formed a layer at the top of the liquid.

Imaging flow cytometry (ImageStream)

After digestion, the mature adipocytes were transferred to microtubes, and samples were run on an ImageStream X Mark II (Amnis part of Luminex) that combines flow cytometry with detailed cell imaging and functional studies. A ×40 magnification was used for all acquisitions. Data were acquired with INSPIRE software (Amnis part of Luminex) and analyzed with IDEAS software (v6.2, Amnis part of Luminex).

Insulin stimulation

Mature adipocytes were treated with 120 nM of insulin (Sigma-Aldrich, reference no. I9278) for 0, 5, 10, 15, 30, and 60 min. Imaging flow cytometry was performed to quantify the membrane expression of GLUT4 by using an Alexa Fluor 594 anti-GLUT4 antibody (Novus, reference no. NBP1-49533). Images (×40 magnification) were processed with computer software. Focused cells were selected using gradient root mean square, and single cells were

gated using area and aspect ratio. Unsaturated Alexa Fluor 594 GLUT4 images were gated by using the Raw Max Pixel feature for the channel 04. Discrimination of adipocytes from debris was achieved using the Raw Max Pixel_MC_SSC versus Max Pixel_MC_SSC features (adipocytes display high values for both parameters). Quantification of membrane GLUT4 was determined by using the Mean Pixel feature in the input mask "Dilate(LevelSet(M01, 1-Brightfield, Dim, 5), 2)." The mean pixel feature is computed as intensity/number of pixels for the GLUT4 staining in this specific mask. At least 200 focused single adipocytes were analyzed for each type of mice. Glucose uptake was performed with flow cytometry with the Assay Genie Kit (reference no. BN00905) and analyzed with Sony SP6800 and Sony SP6800 software after 120 nM insulin stimulation at 0, 5, 10, 15, 30, and 60 min.

Fibroblast culture

Fibroblasts were collected from *PIK3CA*^{WT} and *PIK3CA*$^{CAGG\text{-}CreER}$ mice using standard methods (*17*). To generate dermal fibroblast cultures, skin samples were minced and incubated at room temperature in 0.05% trypsin-EDTA (Thermo Fisher Scientific) solution for 30 min with gentle shaking. Cells were collected by centrifugation at 500*g* for 10 min, resuspended in cell culture medium containing 20% FBS, and plated in a T25 flask to establish lines. Fibroblast cultures were grown and maintained in 1× Dulbecco's modified Eagle's medium (Gibco) supplemented with 20% FBS and penicillin/streptomycin (Gibco), with a final concentration of 100 IU of penicillin and amphotericin B (500 μg ml^{-1}). Cells at similar population doublings were plated 1:4 from confluent cultures and allowed to grow until ~80% confluence was achieved. The cells were seeded in 24-well tissue culture plates at 5×10^4 cells per well. Then, the medium was replaced with medium containing 4-OH tamoxifen (1 μM; Sigma-Aldrich) for 48 hours to activate Cre recombinase.

Targeted liquid chromatography–mass spectrometry metabolites analyses

Blood samples were obtained in EDTA tubes for plasma analysis and EDTA-free tubes for serum analysis. Plasma and serum were obtained after centrifugation of the blood at 500*g* for 10 min. Cell, plasma, and serum samples were immediately snap-frozen in liquid nitrogen. For the liquid chromatography–mass spectrometry (LC-MS) analyses, metabolites were extracted as follows. The extraction solution was composed of 50% methanol (MeOH), 30% acetonitrile, and 20% water. The volume of the added extraction solution was adjusted to the cell number (1 ml per 1 million cells) or plasma and serum volume (200 μl per 10 μl of plasma or serum). After the addition of extraction solution, samples were vortexed for 5 min at 4°C and then centrifuged at 16,000*g* for 15 min at 4°C. The supernatants were collected and stored at −80°C until the analyses were performed. LC-MS analyses were conducted using a Q Exactive Plus Orbitrap mass spectrometer equipped with an Ion Max source and a HESI II probe coupled to the Dionex UltiMate 3000 UPLC System (Thermo Fisher Scientific). External mass calibration was performed using the standard calibration mixture every 7 days as recommended by the manufacturer. Five microliters of each sample was injected onto ZIC-pHILIC [150 mm × 2.1 mm inner diameter (i.d.), 5 μm] with the guard column (20 mm × 2.1 mm i.d., 5 μm; Millipore) for liquid chromatography separation. Buffer A was 20 mM ammonium carbonate and 0.1% ammonium hydroxide (pH 9.2); buffer B was acetonitrile. The chromatographic gradient was run at a flow rate of 0.200 μl/min as follows: for 0 to 20 min, linear gradient from 80 to 20% B; for 20 to 20.5 min, linear gradient from 20 to 80% B; and for 20.5 to 28 min, hold at 80% B. The mass spectrometer was operated in full-scan polarity switching mode with the spray voltage set to 2.5 kV and the heated capillary held at 320°C. The sheath gas flow was set to 20 U; the auxiliary gas flow was set to 5 U, and the sweep gas flow was set to 0 U. The metabolites were detected across a mass range of 75 to 1000 mass-to-charge ratio (*m/z*) at a resolution of 35,000 (at 200 *m/z*) with the automatic gain control (AGC) target set to 106 and a maximum injection time of 250 ms. Lock masses were used to ensure mass accuracy below 5 parts per million. Data were acquired with Thermo Xcalibur 4.0.27.13 software (Thermo Fisher Scientific). The peak areas of metabolites were determined using Thermo TraceFinder 3.3 SP1 software (Thermo Fisher Scientific) and identified by the exact mass of each singly charged ion and by known retention time in the high-performance liquid chromatography (HPLC) column.

LC-MS analysis of alpelisib

Each tissue type was homogenized in 100% cold MeOH with tissue-to-solvent ratio of 1-mg tissue to 5-μl MeOH. After sonication of 20 s, the tissue extract was centrifuged at 13,000*g* for 30 min and then injected onto a Phenomenex Kinetex XB-C18 HPLC column (100 mm by 2.1 mm) at 45°C. Alpelisib was analyzed by reverse-phase HPLC (Shimadzu LCMS system 8040 interfaced with the LabSolutions software). Twenty micrograms of tissue extracts was injected onto a column, and the mobile phase used for the separation consisted of two eluants: Solvent A was 0.1% formic acid in ddH_2O, and solvent B was acetonitrile with 0.1% of formic acid. Compounds were separated by the following discontinuous gradient at a flow rate of 0.6 ml/min: The initial concentration of 20% in solvent B increase to 70% over 6 min, and this was followed by a decrease to 20% over the next minute, and the initial conditions were then maintained for 14 min. The alpelisib was monitored spectrophotometrically by absorbance (photodiode detector) from 205 to 600 nm and by tandem mass detection. The mass measurement was implemented in positive ion mode using multiple reaction monitoring (MRM) with an electrospray ionization source. Three MRM transitions for alpelisib are used as follows: 442.1 > 328.0, 442.1 > 288.0, and 442.1 > 115.1. The quantification was done by integration of the peak absorbance area using a calibration curve established with various known concentrations of alpelisib.

Patients

Following procedures previously described in (*43*), the study was conducted on 12 patients, including 8 children and 6 females who were followed at Hôpital Necker-Enfants Malades. This protocol was approved by the Agence Nationale de Sécurité du Médicament et des Produits de Santé. Written informed consent was obtained from adult patients and from the parents of pediatric patients. Alpelisib was compassionately offered by Novartis. Adult patients received 250 mg/day, and pediatric patients received 50 mg/day (*17*). Alpelisib was taken orally every morning during breakfast. Patients were assessed at regular intervals as previously reported (*17*). When possible, we assessed the volume of adipose tissue overgrowth using MRI for each patient. Magnetoresistance examination was performed using T1, T2, and fat suppression, and T2-weighted

imaging sequences were performed before alpelisib (day 0) introduction and again 6 months after. Volumetric evaluation of adipose tissue malformation was determined by thresholding and manually delineating hypersignal T2 lesions. Volume was calculated by summing images based on the 2D contours and slice thickness.

Data analysis and statistics

Data were expressed as means ± SEM. Survival curves were analyzed with the Mantel-Cox (log-rank) test. Differences between the experimental groups were evaluated using analysis of variance (ANOVA), followed by Tukey-Kramer post hoc test when the results were significant ($P < 0.05$). When only two groups were compared, Mann-Whitney tests were used. The statistical analysis was performed using GraphPad Prism software (version 7.0a).

Supplementary Materials

This PDF file includes:

Figs. S1 to S21
Tables S1 and S2

REFERENCES AND NOTES

1. K. M. Keppler-Noreuil, J. J. Rios, V. E. Parker, R. K. Semple, M. J. Lindhurst, J. C. Sapp, A. Alomari, M. Ezaki, W. Dobyns, L. G. Biesecker, PIK3CA-related overgrowth spectrum (PROS): Diagnostic and testing eligibility criteria, differential diagnosis, and evaluation. *Am. J. Med. Genet. A* **167A**, 287–295 (2015).
2. K. C. Kurek, V. L. Luks, U. M. Ayturk, A. I. Alomari, S. J. Fishman, S. A. Spencer, J. B. Mulliken, M. E. Bowen, G. L. Yamamoto, H. P. Kozakewich, M. L. Warman, Somatic mosaic activating mutations in PIK3CA cause CLOVES syndrome. *Am. J. Hum. Genet.* **90**, 1108–1115 (2012).
3. B. Bilanges, Y. Posor, B. Vanhaesebroeck, PI3K isoforms in cell signalling and vesicle trafficking. *Nat. Rev. Mol. Cell Biol.* **20**, 515–534 (2019).
4. H. C. Welch, W. J. Coadwell, L. R. Stephens, P. T. Hawkins, Phosphoinositide 3-kinase-dependent activation of Rac. *FEBS Lett.* **546**, 93–97 (2003).
5. K. M. Keppler-Noreuil, J. C. Sapp, M. J. Lindhurst, V. E. Parker, C. Blumhorst, T. Darling, L. L. Tosi, S. M. Huson, R. W. Whitehouse, E. Jakkula, I. Grant, M. Balasubramanian, K. E. Chandler, J. L. Fraser, Z. Gucev, Y. J. Crow, L. M. Brennan, R. Clark, E. A. Sellars, L. D. Pena, V. Krishnamurty, A. Shuen, N. Braverman, M. L. Cunningham, V. R. Sutton, V. Tasic, J. M. Graham Jr., J. Geer Jr., A. Henderson, R. K. Semple, L. G. Biesecker, Clinical delineation and natural history of the PIK3CA-related overgrowth spectrum. *Am. J. Med. Genet. A* **164A**, 1713–1733 (2014).
6. G. Canaud, A. M. Hammill, D. Adams, M. Vikkula, K. M. Keppler-Noreuil, A review of mechanisms of disease across PIK3CA-related disorders with vascular manifestations. *Orphanet J. Rare Dis.* **16**, 306 (2021).
7. G. Morin, G. Canaud, Treatment strategies for mosaic overgrowth syndromes of the PI3K-AKT-mTOR pathway. *Br. Med. Bull.* **140**, 36–49 (2021).
8. V. L. Luks, N. Kamitaki, M. P. Vivero, W. Uller, R. Rab, J. V. Bovee, K. L. Rialon, C. J. Guevara, A. I. Alomari, A. K. Greene, S. J. Fishman, H. P. Kozakewich, R. A. Maclellan, J. B. Mulliken, R. Rahbar, S. A. Spencer, C. C. Trenor III, J. Upton, D. Zurakowski, J. A. Perkins, A. Kirsh, J. T. Bennett, W. B. Dobyns, K. C. Kurek, M. L. Warman, S. A. McCarroll, R. Murillo, Lymphatic and other vascular malformative/overgrowth disorders are caused by somatic mutations in PIK3CA. *J. Pediatr.* **166**, e1041–e1045 (2015).
9. G. M. Mirzaa, R. L. Conway, K. W. Gripp, T. Lerman-Sagie, D. H. Siegel, L. S. deVries, D. Lev, N. Kramer, E. Hopkins, J. M. Graham, W. B. Dobyns, Megalencephaly-capillary malformation (MCAP) and megalencephaly-polydactyly-polymicrogyria-hydrocephalus (MPPH) syndromes: Two closely related disorders of brain overgrowth and abnormal brain and body morphogenesis. *Am. J. Med. Genet. A* **158A**, 269–291 (2012).
10. J. J. Rios, N. Paria, D. K. Burns, B. A. Israel, R. Cornelia, C. A. Wise, M. Ezaki, Somatic gain-of-function mutations in PIK3CA in patients with macrodactyly. *Hum. Mol. Genet.* **22**, 444–451 (2013).
11. J. B. Rivière, G. M. Mirzaa, B. J. O'Roak, M. Beddaoui, D. Alcantara, R. L. Conway, J. St-Onge, J. A. Schwartzentruber, K. W. Gripp, S. M. Nikkel, T. Worthylake, C. T. Sullivan, T. R. Ward, H. E. Butler, N. A. Kramer, B. Albrecht, C. M. Armour, L. Armstrong, O. Caluseriu, C. Cytrynbaum, B. A. Drolet, A. M. Innes, J. L. Lauzon, A. E. Lin, G. M. Mancini, W. S. Meschino, J. D. Reggin, A. K. Saggar, T. Lerman-Sagie, G. Uyanik, R. Weksberg, B. Zirn, C. L. Beaulieu, J. Majewski, D. E. Bulman, M. O'Driscoll, J. Shendure, J. M. Graham Jr., K. M. Boycott, W. B. Dobyns; Finding of Rare Disease Genes (FORGE) Canada Consortium, De novo germline and postzygotic mutations in AKT3, PIK3R2 and PIK3CA cause a spectrum of related megalencephaly syndromes. *Nat. Genet.* **44**, 934–940 (2012).
12. M. J. Lindhurst, V. E. Parker, F. Payne, J. C. Sapp, S. Rudge, J. Harris, A. M. Witkowski, Q. Zhang, M. P. Groeneveld, C. E. Scott, A. Daly, S. M. Huson, L. L. Tosi, M. L. Cunningham, T. N. Darling, J. Geer, Z. Gucev, V. R. Sutton, C. Tziotzios, A. K. Dixon, T. Helliwell, S. O'Rahilly, D. B. Savage, M. J. Wakelam, I. Barroso, L. G. Biesecker, R. K. Semple, Mosaic overgrowth with fibroadipose hyperplasia is caused by somatic activating mutations in PIK3CA. *Nat. Genet.* **44**, 928–933 (2012).
13. S. M. Leiter, V. E. R. Parker, A. Welters, R. Knox, N. Rocha, G. Clark, F. Payne, L. Lotta, J. Harris, J. Guerrero-Fernández, I. González-Casado, S. García-Miñaur, G. Gordo, N. Wareham, V. Martínez-Glez, M. Allison, S. O'Rahilly, I. Barroso, T. Meissner, S. Davies, K. Hussain, K. Temple, A. C. Barreda-Bonis, S. Kummer, R. K. Semple, Hypoinsulinaemic, hypoketotic hypoglycaemia due to mosaic genetic activation of PI3-kinase. *Eur. J. Endocrinol.* **177**, 175–186 (2017).
14. S. Davis, M. A. Ware, J. Zeiger, M. A. Deardorff, K. Grand, A. Grimberg, S. Hsu, M. Kelsey, S. Majidi, R. P. Matthew, M. Napier, N. Nokoff, C. Prasad, A. C. Riggs, M. L. McKinnon, G. Mirzaa, Growth hormone deficiency in megalencephaly-capillary malformation syndrome: An association with activating mutations in PIK3CA. *Am. J. Med. Genet. A* **182**, 162–168 (2020).
15. H. R. Christofk, M. G. Vander Heiden, M. H. Harris, A. Ramanathan, R. E. Gerszten, R. Wei, M. D. Fleming, S. L. Schreiber, L. C. Cantley, The M2 splice isoform of pyruvate kinase is important for cancer metabolism and tumour growth. *Nature* **452**, 230–233 (2008).
16. G. Morin, C. Degrugillier-Chopinet, M. Vincent, A. Fraissenon, H. Aubert, C. Chapelle, C. Hoguin, F. Dubos, B. Catteau, F. Petit, A. Mezel, O. Domanski, G. Herbreteau, M. Alesandrini, N. Boddaert, N. Boutry, C. Broissand, T. K. Han, F. Branle, S. Sarnacki, T. Blanc, L. Guibaud, G. Canaud, Treatment of two infants with PIK3CA-related overgrowth spectrum by alpelisib. *J. Exp. Med.* **219**, e20212148 (2022).
17. Q. Venot, T. Blanc, S. H. Rabia, L. Berteloot, S. Ladraa, J. P. Duong, E. Blanc, S. C. Johnson, C. Hoguin, O. Boccara, S. Sarnacki, N. Boddaert, S. Pannier, F. Martinez, S. Magassa, J. Yamaguchi, B. Knebelmann, P. Merville, N. Grenier, D. Joly, V. Cormier-Daire, C. Michot, C. Bole-Feysot, A. Picard, V. Soupre, S. Lyonnet, J. Sadoine, L. Slimani, C. Chaussain, C. Laroche-Raynaud, L. Guibaud, C. Broissand, J. Amiel, C. Legendre, F. Terzi, G. Canaud, Targeted therapy in patients with PIK3CA-related overgrowth syndrome. *Nature* **558**, 540–546 (2018).
18. M. D. Muzumdar, B. Tasic, K. Miyamichi, L. Li, L. Luo, A global double-fluorescent Cre reporter mouse. *Genesis* **45**, 593–605 (2007).
19. R. E. Duncan, M. Ahmadian, K. Jaworski, E. Sarkadi-Nagy, H. S. Sul, Regulation of lipolysis in adipocytes. *Annu. Rev. Nutr.* **27**, 79–101 (2007).
20. M. R. Calera, C. Martinez, H. Liu, A. K. Jack, M. J. Birnbaum, P. F. Pilch, Insulin increases the association of Akt-2 with Glut4-containing vesicles. *J. Biol. Chem.* **273**, 7201–7204 (1998).
21. H. Cho, J. Mu, J. K. Kim, J. L. Thorvaldsen, Q. Chu, E. B. Crenshaw III, K. H. Kaestner, M. S. Bartolomei, G. I. Shulman, M. J. Birnbaum, Insulin resistance and a diabetes mellitus-like syndrome in mice lacking the protein kinase Akt2 (PKB beta). *Science* **292**, 1728–1731 (2001).
22. S. S. Bae, H. Cho, J. Mu, M. J. Birnbaum, Isoform-specific regulation of insulin-dependent glucose uptake by Akt/protein kinase B. *J. Biol. Chem.* **278**, 49530–49536 (2003).
23. Z. Y. Jiang, Q. L. Zhou, K. A. Coleman, M. Chouinard, Q. Boese, M. P. Czech, Insulin signaling through Akt/protein kinase B analyzed by small interfering RNA-mediated gene silencing. *Proc. Natl. Acad. Sci. U.S.A.* **100**, 7569–7574 (2003).
24. S. Virtue, A. Vidal-Puig, GTTs and ITTs in mice: Simple tests, complex answers. *Nat. Metab.* **3**, 883–886 (2021).
25. A. M. Cotterill, J. M. Holly, J. A. Wass, The regulation of insulin-like growth factor binding protein (IGFBP)-1 during prolonged fasting. *Clin. Endocrinol. (Oxf)* **39**, 357–362 (1993).
26. A. J. Levine, A. M. Puzio-Kuter, The control of the metabolic switch in cancers by oncogenes and tumor suppressor genes. *Science* **330**, 1340–1344 (2010).
27. N. N. Pavlova, C. B. Thompson, The emerging hallmarks of cancer metabolism. *Cell Metab.* **23**, 27–47 (2016).
28. R. J. DeBerardinis, N. S. Chandel, Fundamentals of cancer metabolism. *Sci. Adv.* **2**, e1600200 (2016).
29. C. Kurlawalla-Martinez, B. Stiles, Y. Wang, S. U. Devaskar, B. B. Kahn, H. Wu, Insulin hypersensitivity and resistance to streptozotocin-induced diabetes in mice lacking PTEN in adipose tissue. *Mol. Cell. Biol.* **25**, 2498–2510 (2005).
30. J. Magdalon, S. M. Sánchez-Sánchez, K. Griesi-Oliveira, A. L. Sertié, Dysfunctional mTORC1 signaling: A convergent mechanism between syndromic and nonsyndromic forms of autism spectrum disorder? *Int. J. Mol. Sci.* **18**, 659 (2017).
31. K. Hussain, B. Challis, N. Rocha, F. Payne, M. Minic, A. Thompson, A. Daly, C. Scott, J. Harris, B. J. Smillie, D. B. Savage, U. Ramaswami, P. De Lonlay, S. O'Rahilly, I. Barroso, R. K. Semple, An activating mutation of AKT2 and human hypoglycemia. *Science* **334**, 474 (2011).

32. M. Minic, N. Rocha, J. Harris, M. P. Groeneveld, S. Leiter, N. Wareham, A. Sleigh, P. De Lonlay, K. Hussain, S. O'Rahilly, R. K. Semple, Constitutive activation of AKT2 in humans leads to hypoglycemia without fatty liver or metabolic dyslipidemia. *J. Clin. Endocrinol. Metab.* **102**, 2914–2921 (2017).
33. D. Alcantara, A. E. Timms, K. Gripp, L. Baker, K. Park, S. Collins, C. Cheng, F. Stewart, S. G. Mehta, A. Saggar, L. Sztriha, M. Zombor, O. Caluseriu, R. Mesterman, M. I. Van Allen, A. Jacquinet, S. Ygberg, J. A. Bernstein, A. M. Wenger, H. Guturu, G. Bejerano, N. Gomez-Ospina, A. Lehman, E. Alfei, C. Pantaleoni, V. Conti, R. Guerrini, U. Moog, J. M. Graham Jr., R. Hevner, W. B. Dobyns, M. O'Driscoll, G. M. Mirzaa, Mutations of AKT3 are associated with a wide spectrum of developmental disorders including extreme megalencephaly. *Brain* **140**, 2610–2622 (2017).
34. N. Koundouros, E. Karali, A. Tripp, A. Valle, P. Inglese, N. J. S. Perry, D. J. Magee, S. Anjomani Virmouni, G. A. Elder, A. L. Tyson, M. L. Doria, A. van Weverwijk, R. F. Soares, C. M. Isacke, J. K. Nicholson, R. C. Glen, Z. Takats, G. Poulogiannis, Metabolic fingerprinting links oncogenic PIK3CA with enhanced arachidonic acid-derived eicosanoids. *Cell* **181**, 1596–1611 e1527 (2020).
35. S. D. Castillo, E. Tzouanacou, M. Zaw-Thin, I. M. Berenjeno, V. E. Parker, I. Chivite, M. Milà-Guasch, W. Pearce, I. Solomon, A. Angulo-Urarte, A. M. Figueiredo, R. E. Dewhurst, R. G. Knox, G. R. Clark, C. L. Scudamore, A. Badar, T. L. Kalber, J. Foster, D. J. Stuckey, A. L. David, W. A. Phillips, M. F. Lythgoe, V. Wilson, R. K. Semple, N. J. Sebire, V. A. Kinsler, M. Graupera, B. Vanhaesebroeck, Somatic activating mutations in Pik3ca cause sporadic venous malformations in mice and humans. *Sci. Transl. Med.* **8**, 332ra343 (2016).
36. H. Kondo, C. D. H. Ratcliffe, S. Hooper, J. Ellis, J. I. MacRae, M. Hennequart, C. W. Dunsby, K. I. Anderson, E. Sahai, Single-cell resolved imaging reveals intra-tumor heterogeneity in glycolysis, transitions between metabolic states, and their regulatory mechanisms. *Cell Rep.* **34**, 108750 (2021).
37. V. Rajeeve, W. Pearce, M. Cascante, B. Vanhaesebroeck, P. R. Cutillas, Polyamine production is downstream and upstream of oncogenic PI3K signalling and contributes to tumour cell growth. *Biochem. J.* **450**, 619–628 (2013).
38. I. Martinez-Reyes, N. S. Chandel, Cancer metabolism: Looking forward. *Nat. Rev. Cancer* **21**, 669–680 (2021).
39. G. Hoxhaj, B. D. Manning, The PI3K-AKT network at the interface of oncogenic signalling and cancer metabolism. *Nat. Rev. Cancer* **20**, 74–88 (2020).
40. R. R. Madsen, B. Vanhaesebroeck, R. K. Semple, Cancer-associated PIK3CA mutations in overgrowth disorders. *Trends Mol. Med.* **24**, 856–870 (2018).
41. C. E. Lau, G. D. Tredwell, J. K. Ellis, E. W. Lam, H. C. Keun, Metabolomic characterisation of the effects of oncogenic PIK3CA transformation in a breast epithelial cell line. *Sci. Rep.* **7**, 46079 (2017).
42. B. Faubert, A. Solmonson, R. J. DeBerardinis, Metabolic reprogramming and cancer progression. *Science* **368**, eaaw5473 (2020).
43. F. Delestre, Q. Venot, C. Bayard, A. Fraissenon, S. Ladraa, C. Hoguin, C. Chapelle, J. Yamaguchi, R. Cassaca, L. Zerbib, S. Magassa, G. Morin, V. Asnafi, P. Villarese, S. Kaltenbach, S. Fraitag, J. P. Duong, C. Broissand, O. Boccara, V. Soupre, B. Bonnotte, C. Chopinet, T. Mirault, C. Legendre, L. Guibaud, G. Canaud, Alpelisib administration reduced lymphatic malformations in a mouse model and in patients. *Sci. Transl. Med.* **13**, eabg0809 (2021).
44. A. Klippel, C. Reinhard, W. M. Kavanaugh, G. Apell, M. A. Escobedo, L. T. Williams, Membrane localization of phosphatidylinositol 3-kinase is sufficient to activate multiple signal-transducing kinase pathways. *Mol. Cell. Biol.* **16**, 4117–4127 (1996).
45. L. Srinivasan, Y. Sasaki, D. P. Calado, B. Zhang, J. H. Paik, R. A. DePinho, J. L. Kutok, J. F. Kearney, K. L. Otipoby, K. Rajewsky, PI3 kinase signals BCR-dependent mature B cell survival. *Cell* **139**, 573–586 (2009).
46. A. Fedorov, R. Beichel, J. Kalpathy-Cramer, J. Finet, J. C. Fillion-Robin, S. Pujol, C. Bauer, D. Jennings, F. Fennessy, M. Sonka, J. Buatti, S. Aylward, J. V. Miller, S. Pieper, R. Kikinis, 3D slicer as an image computing platform for the quantitative imaging network. *Magn. Reson. Imaging* **30**, 1323–1341 (2012).
47. P. Bankhead, M. B. Loughrey, J. A. Fernandez, Y. Dombrowski, D. G. McArt, P. D. Dunne, S. McQuaid, R. T. Gray, L. J. Murray, H. G. Coleman, J. A. James, M. Salto-Tellez, P. W. Hamilton, QuPath: Open source software for digital pathology image analysis. *Sci. Rep.* **7**, 16878 (2017).
48. C. Stringer, T. Wang, M. Michaelos, M. Pachitariu, Cellpose: A generalist algorithm for cellular segmentation. *Nat. Methods* **18**, 100–106 (2021).
49. J. Schindelin, I. Arganda-Carreras, E. Frise, V. Kaynig, M. Longair, T. Pietzsch, S. Preibisch, C. Rueden, S. Saalfeld, B. Schmid, J. Y. Tinevez, D. J. White, V. Hartenstein, K. Eliceiri, P. Tomancak, A. Cardona, Fiji: An open-source platform for biological-image analysis. *Nat. Methods* **9**, 676–682 (2012).
50. S. Berg, D. Kutra, T. Kroeger, C. N. Straehle, B. X. Kausler, C. Haubold, M. Schiegg, J. Ales, T. Beier, M. Rudy, K. Eren, J. I. Cervantes, B. Xu, F. Beuttenmueller, A. Wolny, C. Zhang, U. Koethe, F. A. Hamprecht, A. Kreshuk, ilastik: Interactive machine learning for (bio)image analysis. *Nat. Methods* **16**, 1226–1232 (2019).
51. S. Mailfert, J. Touvier, L. Benyoussef, R. Fabre, A. Rabaoui, M. C. Blache, Y. Hamon, S. Brustlein, S. Monneret, D. Marguet, N. Bertaux, A theoretical high-density nanoscopy study leads to the design of UNLOC, a parameter-free algorithm. *Biophys. J.* **115**, 565–576 (2018).

Acknowledgments

Funding: This study was supported by the European Research Council (CoG 2020 grant number 101000948 awarded to G.C.), the Agence Nationale de la Recherche—Programme d'Investissements d'Avenir (ANR-18-RHUS-005 to G.C.), and the Agence Nationale de la Recherche—Programme de Recherche Collaborative (19-CE14-0030-01 to G.C.). This work was also supported by the CLOVES Syndrome Community (West Kennebunk, USA), Association Syndrome de CLOVES (Nantes, France), Fondation d'entreprise IRCEM (Roubaix, France), Fonds de dotation Emmanuel BOUSSARD (Paris, France), the Fondation DAY SOLVAY (Paris, France), the Fondation TOURRE (Paris, France) to G.C., the Fondation BETTENCOURT SCHUELLER (Paris, France) to G.C., the Fondation Simone et Cino DEL DUCA (Paris, France), the Fondation Line RENAUD-Loulou GASTE (Paris, France), the Fondation Schlumberger pour l'Education et la Recherche (Paris, France), the Association Robert Debré pour la Recherche Médicale awarded to G.C., WonderFIL smiles—A Facial Infiltrating Lipomatosis community (Norway), INSERM, Assistance Publique Hôpitaux de Paris, l'Université Paris Cité and Fondation pour la Recherche Médicale (FDM202006011222) awarded to G.M., and Banting Postdoctoral Fellowship (Canadian Institutes of Health Research, #472149) awarded to A.P.G. We are also very grateful to our generous donors. In vivo preclinical imaging was performed at the Life Imaging Facility of the University of Paris (Plateforme Imageries du Vivant), supported by France Life Imaging (grant ANR-11-INBS-0006) and Infrastructures BiologieSanté (IBISA). **Author contributions:** S.L., C.Ba., L.Z., Q.V., G.M., A.P.G., M.D., C.C.-G., and J.De. performed the experiments, analyzed the data, and elaborated figures. A.F. and L.G. designed and analyzed MRI experiments. C.H. and C.C. were in charge of mice experiments including genotyping, breeding, tamoxifen administration, and sacrifice. V.A., P.V., and S.K. performed molecular diagnosis in patients. P.I., S.F., J.-P.D., and J.B. analyzed mice and human tissues section. I.N., J.-M.L., and P.L. performed the metabolomic analysis. M.Pe. provided input on the manuscript. T.V. performed the FDG uptake experiments. G.A. and B.T. performed mouse MRI experiments. J.Da. performed LC-MS experiments. N.G. designed the plugin for immunostaining quantification. C.Br., A.B., M.Po., and C.L. followed patients and participated in data analysis. G.C. followed the patients, provided the conceptual framework, designed the study, supervised the project, and wrote the paper. **Competing interests:** A patent application ["BYL719 (alpelisib) for use in the treatment of PIK3CA-related overgrowth spectrum" #WO2017140828A1] has been filed by INSERM (Institut National de la Santé et de la Recherche Médicale), Centre National De La Recherche Scientifique (CNRS), Université Paris Cité, and Assistance Publique-Hôpitaux De Paris (AP-HP) for the use of BYL719 (alpelisib) in the treatment of *PIK3CA*-related overgrowth spectrum (PROS/CLOVES syndrome). G.C. is the inventor. This patent is licensed to Novartis. A patent application ("Methods for monitoring and treating Warburg effect in patients with PI3K-related disorders," #EP22305091) has been filed by INSERM (Institut National de la Santé et de la Recherche Médicale), CNRS, Université Paris Cité, and AP-HP for the monitoring and treatment of Warburg effect in patients with PI3K-related disorders. G.C. and S.L. are the inventors. G.C. receives or has received consulting fees from Novartis, Fresenius Medical Care, Vaderis, Alkermes, IPSEN, and BridgeBio. The other authors declare that they have no other competing interests. **Data and materials availability:** All data needed to evaluate the conclusions in the paper are present in the paper and/or the Supplementary Materials.

Submitted 7 September 2022
Accepted 3 November 2022
Published 9 December 2022
10.1126/sciadv.ade7823

ScienceAdvances

PIK3CA gain-of-function mutation in adipose tissue induces metabolic reprogramming with Warburg-like effect and severe endocrine disruption

Sophia LadraaLola ZerbibCharles BayardAntoine FraissenonQuitterie VenotGabriel MorinAlexandre P. GarneauPierre IsnardCélia ChapelleClément HoguinSylvie FraitagJean-Paul DuongLaurent GuibaudAlix BesançonSophie KaltenbachPatrick VillareseVahid AsnafiChristine BroissandNicolas GoudinMichael DussiotIvan NemazanyyThomas VielGwennhael AutretCéline Cruciani-GuglielmacciJessica DenomJulie BruneauBertrand TavitianChristophe LegendreJulien DairouJean-Marc LacortePacifique LevyMario PendeMichel PolakGuillaume Canaud

Sci. Adv., 8 (49), eade7823. • DOI: 10.1126/sciadv.ade7823

Science Advances (ISSN) is published by the American Association for the Advancement of Science. 1200 New York Avenue NW, Washington, DC 20005. The title *Science Advances* is a registered trademark of AAAS.